Fibers **2015**, *3*, 103-133; doi:10.3390/fib3020103

OPEN ACCESS
fibers
ISSN 2079-6439
www.mdpi.com/journal/fibers

Article

In Situ Hybridization of Pulp Fibers Using Mg-Al Layered Double Hydroxides

Carl-Erik Lange [1,*], Mika Lastusaari [2,3], Mehedi Reza [4], Seyed Kourosh Latifi [5], Pasi Kallio [5] and Pedro Fardim [1,*]

[1] Department of Chemical Engineering, Åbo Akademi University, Porthansgatan 3-5, FI-20500 Åbo, Finland
[2] Department of Chemistry, University of Turku, FI-20014 Turun Yliopisto, Finland; E-Mail: miklas@utu.fi
[3] Turku University Centre for Materials and Surfaces (MatSurf), FI-20014 Turun Yliopisto, Finland
[4] Department of Applied Physics, Aalto University School of Science, FI-00076 Aalto, Finland; E-Mail: mehedi.reza@aalto.fi
[5] Department of Automation Science and Engineering, Tampere University of Technology, Korkeakoulunkatu 3, FI-33720 Tampere, Finland; E-Mails: kourosh_latifi@hotmail.com (S.K.L.); pasi.kallio@tut.fi (P.K.)

* Authors to whom correspondence should be addressed; E-Mails: clange@abo.fi (C.-E.L.); pfardim@abo.fi (P.F.); Tel.: +358-2-2154237 (C.-E.L.); +358-50-4096424 (P.F.).

Academic Editor: Noureddine Abidi

Received: 27 February 2015 / Accepted: 13 April 2015 / Published: 29 April 2015

Abstract: Inorganic Mg^{2+} and Al^{3+} containing layered double hydroxide (LDH) particles were synthesised *in situ* from aqueous solution onto chemical pulp fibers of pine (*Pinus sylvestris*). High super saturated (*hss*) solution with sodium carbonate produced LDH particles with an average diameter of 100–200 nm. Nano-size (70 nm) LDH particles were found from fibers external surface and, to a lesser degree, from the S2 cell wall after synthesis via low super saturated (*lss*) route. The synthesis via slow urea hydrolysis (*Uhyd*) yielded micron and clay sized LDH (2–5 μm) and enabled efficient fiber densification via mineralization of S2 fiber wall layer as indicated by TEM and compliance analysis. The *Uhyd* method decreased fiber compliance up to 50%. Reduction in the polymerisation degree of cellulose was observed with capillary viscometry. Thermogravimetric analysis showed that the hybridization with LDH reduced the exothermic heat, indicating, that this material can be incorporated in flame retardant applications. Fiber charge was assessed by

adsorption expermients with methylene blue (MB) and metanil yellow (MY). Synthesis via *lss* route retained most of the fibres original charge and provided the highest capacity (10 μmol/g) for anionic MY, indicating cationic character of hybrid fibers. Our results suggested that mineralized fibers can be potentially used in advanced applications such as biocomposites and adsorbent materials.

Keywords: combustion; compliance; flexibility; FTIR; kraft; mineralization; pine; pulp; SEM; TEM

1. Introduction

A great deal of research that concentrates on layered double hydroxide (LDH) particles is related to composite structures with various polymeric matrices [1,2] and sorption processes for water purification applications [3,4], but also to coating technology, especially in corrosion protection [5–7], and to different catalytic processes [8,9]. Electrochemical applications, such as batteries [10], capacitors [11] and electrodes [12], in which thin film structures are important [5], are of interest, as well. Some studies have emerged around the pulp and paper industry. Applications that involve packaging materials [13–15], bleaching [16], filler formulation [17] and lignin depolymerization [18] are being devised. Many of these research fields require material scientists to expand the LDH structure beyond the simple hydrotalcite (HT) that is comprised of Mg^{2+} and Al^{3+} hydroxides and CO_3^{2-} as a counter balancing ion residing within the interlamellar gallery. Other synthesized natural-like minerals that are included in the hydrotalcite group are the ones where Mg^{2+} is replaced by Zn^{2+} [19–21] as in zaccagnaite or by Ni^{2+} [22,23] as in takovite. Trivalent aluminum may be replaced by Fe^{3+} [24,25] as in pyroaurite or reevesite. Furthermore, post-synthetic processing of LDH is often applied to facilitate desirable properties. These processes include calcination, anion exchange, reconstruction and exfoliation [1,8,26].

Considering the synthesis, the nucleation kinetics in high supersaturated solution (*hss*) generally produces LDH particles with lower crystallinity, since the number of nucleation sites is at the maximum in the given system and the pH changes strongly at the beginning of synthesis [27]. In low supersaturated solution (*lss*) conditions, the crystal growth surpasses nucleation. Slow titration provides nano-sized particles and better formed crystals, due to continuous pH control. The size of inorganic particles that are synthesized in aqueous solution can be affected via post-synthetic hydrothermal treatment. Elevated temperature and pressure allows cations to migrate slowly in the crystalline structure of an LDH. For example, the slow urea hydrolysis (*Uhyd*) produces micron-sized particles due to an ammonia-induced slow pH increase [20]. Since LDH particles are known for their memory effect upon calcination and being capable of exchanging gallery ions in order of stability, faults and perturbations in the crystalline structure may allow the particles to remain active, even if carbonate is being introduced into the lattice during the synthesis.

For any engineered application where wood fibers are deployed, it is important to understand the changes in their fundamental characteristics during processing. We have previously shown how the surface chemistry of fibers can be changed with LDH and how these fibers behave in injection molded

composite structures [28,29]. In this article, we address the chemical and physical characteristics of pulp fibers considering the changes in cellulose polymer chain length, adsorption capacity, thermal behavior and compliance after the *lss*, *hss* and *Uhyd* synthesis routes, which all involve *in situ* LDH particle synthesis on fiber surfaces. To our surprise, the *Uhyd* synthesis was able to mineralize the fibers, as well.

2. Experimental Section

2.1. Materials

Chemicals that were supplied by Sigma-Aldrich (Saint Louis, MO, USA) include aluminium nitrate ($Al(NO_3)_3 \cdot 9H_2O$, $\geq$ 98%, Germany), hydrotalcite (HT) that was used as a reference LDH ($Mg_6Al_2(CO_2)(OH)_{16} \cdot 4H_2O$, USA) magnesium nitrate ($Mg(NO_3)_2 \cdot 6H_2O$, 98%–102%, UK), metanil yellow (MY) ($C_{18}H_{14}N_3O_3SNa$, $\geq$ 98%, Switzerland) and high purity Zn standard (Zn, $\geq$99.998%, EU). Chemicals purchased from Merck (Kenilworth, NJ, USA) include barbital ($C_8H_{12}N_2O_3$, $\geq$99%, Germany), sodium carbonate (Na_2CO_3, $\geq$99.9%, Germany), potassium chloride (KCl, $\geq$99.5%, Germany) and urea ($CO(NH_2)_2$, $\geq$99.0%–100.5%, Germany). High purity Pb standard (Pb, $\geq$99.998%, US) was supplied by TA Instruments (New Castle, DE, USA). Analyte for methylene blue (MB) ($C_{16}H_{18}ClN_3S \cdot xH_2O$, $\simeq$95%, Switzerland) adsorption was supplied by Ciba. MB was recrystallized from hot deionized water solution with ethanol upon cooling for removal of crystalline water. Bis(ethylenediamine)copper(II) hydroxide (CED) solution ($Cu(NH_2(CH_2)_2NH_2)_2(OH)_2$, 1.0 M, Finland) was purchased from FF-Chemicals (Haukipudas, FIN). Fully bleached chemical sulphate pulp (BKraft) of pine (*Pinus sylvestris*) was kindly provided by Metsä Fiber (Rauma Mill, Finland). All received pulp samples were stored in a freezer and used after thawing in a cooler at 283 K (10 °C). All reagents except MB were used without further purification.

2.2. Methods

2.2.1. LDH Synthesis and Fiber Mineralization

LDH synthesis was carried out in two stages. The precipitation stage was set up according to the chosen synthesis route, namely *lss*, *hss* or *Uhyd*. Two automatic titrators were applied for dispensing the reagents into distilled water in *lss* route. The acidic (pH = 3.7) aqueous solution of $Al(NO_3)_3$ and $Mg(NO_3)_2$ with total metal ion concentration ($c(M^{z+}_{tot})$) equal to 0.50 M at molar ratio 1 : 2 was dispensed from one of the titrators. The pH was kept close to 9.5 by dispensing 1.0 M NaOH from the other. Dispensing rate in monotonous equilibrium titration method was set to 0.33 mL $\cdot$ min^{-1} for both reagents. The suspension was stirred vigorously during the synthesis. Carbonate containing LDH particles was synthesised via *hss* route by adding calculated amount of Na_2CO_3 into the aqueous solution that contained the precipitating ions. Particle nucleation begins immediately after Na_2CO_3 is transferred into the precursors containing solution due to rapid pH change. LDH synthesis via *Uhyd* followed the *hss* with an exception that pH was controlled by slow urea hydrolysis in an autoclave. The $c(M^{z+}_{tot})$ in final reaction volume (500 mL) in all experiments was 25 mM. The amount of added and liberated carbonate in *hss* and *Uhyd* synthesis routes, respectively, was set to $3.3c(M^{z+}_{tot})$, which corresponded to

twenty fold excess from the calculated amount that was required to balance the charge in LDH gallery. To advance the olation and crystallization processes in the second stage the precipiatates were transferred into 1000 mL reaction vessels and treated under hydrothermal conditions with autogeneous pressure built up at 393 ± 10 K (120 ± 10 °C) for 48 h. Urea was assumed to hydrolyse completely in the given conditions. Synthesised LDH were washed several times by centrifugation and concomitant solvent exchange.

Modification of pulp fibers followed the same procedures. Dry weight of applied BKraft fibers was 5.0 g. The pulp sludge in *hss* and *Uhyd* synthesis route were allowed to soak for 90 min in the Al^{3+} and Mg^{2+} nitrate solution prior to hydrothermal treatment. In *lss* the fibers were first disintegrated in distilled water. Finally the pulp samples were thoroughly washed by repetitious filtration through a filter paper (pore size: 7–12 microns) at maximum of 2% suspension consistency in reduced pressure until the UV-Vis analysis from the filtrates showed a change less than 0.01 absorbance units at the dispersion edge (240 nm). The pH of a final filtrate was in between 7.0 and 7.5. Then the pulp fibers were dried in an oven at 333 K (60 °C) until constant weight. Hereafter the modified pulp fibers are referred according to the synthesis procedure (*lss*, *hss* and *Uhyd*). Neat LDH particles are referred to LDH-OH, LDH-C and LDH-U respectively.

2.2.2. X-Ray Diffractometry

X-ray diffractometer (Rigaku MiniFlex-II Desktop X-ray Diffractometer) was used to record the diffraction pattern (XRD) of the neat particles. The XRD patterns were collected in the 2θ range of 2°–40° with CuKα ($\lambda = 1.54184$ Å) radiation. The resolution was 0.02° and the scanning speed was 2° min^{-1}. Operating voltage of the X-ray tube was 30 kV and the electric current was 15 mA.

2.2.3. ATR-FTIR

Infrared spectrophotometer (Thermo Scientific, Nicolet iS50 FT IR, Madison, WI, USA) with attenuated total reflection (ATR) setup was used in analysis of LDH particles and modified pulp fibers at different stages of combustion. Instrument was equipped with a diamond crystal and a pressure gauge. The pressure was set to 30 ± 2 kg in all samples. Total of 64 scans was recorded and corrected with the Omnic® spectral suite software that provided ambient background and ATR correction for 45° incident angle with 1 refraction assuming 1.50 refractive index for all samples.

Combustion was evaluated by heating the sample to the target temperature in a muffle oven in an open porcelain crucible. 10 min conditioning was allowed for the sample that was treated at 473 K (200 °C) while the ones that were treated at higher temperatures were taken out within one minute after target temperature was reached. Temperature ramp rate was $20\ \mathrm{K} \cdot \mathrm{min}^{-1}$. In combustion kinetics the sample was heated from the ambient conditions rapidly to 613 K (340 °C). Cooling down was allowed to occur in a crucible with a lid for approximately two minutes prior to FTIR analysis. The vibration induced absorbance signals were deconvoluted by applying Gaussian fit with Origin® 7.5 software. The rule for minimum number of required absorbance signals was used.

2.2.4. Thermogravimetry

Thermo gravimetric analysis was performed with TA Instruments (SDT 2960, New Castle, DE, USA) apparatus. Thermographs (TG) for LDH powders were recorded by using linear $3\ \mathrm{K} \cdot \mathrm{min}^{-1}$ sweep rate up to 873 K ($600\ ^{\circ}\mathrm{C}$) under constant air flow ($100\ \mathrm{mL} \cdot \mathrm{min}^{-1}$) in aluminium oxide cups ($60\ \mu\mathrm{L}$). The weight of pristine LDH powder in each experiment was approximately 20 mg.

The LDH modified pulp fibers were compressed in a custom made pelletizer to cylindrical shape that was 5.0 ± 0.1 mm in diameter and 0.85 ± 0.05 mm in thickness. The applied pressure ($175 \pm 20\ \mathrm{kg{\cdot}cm}^{-2}$) and the sample weight (10 ± 1 mg) were optimized before TG analysis. Sample density was $600 \pm 50\ \mathrm{kg} \cdot \mathrm{m}^{-3}$. The pellets were designed to allow enough porosity for gaseous combustion products to leave the sample upon heating. The thermal history of the pulp samples was controlled with an isotherm at 473 K ($200\ ^{\circ}\mathrm{C}$). After 10 min isothermal conditioning the linear sweep was allowed to continue as with LDH powders up to 800 K ($527\ ^{\circ}\mathrm{C}$) where another isotherm was commenced for 10 min to stabilize the weight of residual LDH. Baseline was defined by recording the thermograph with an empty alumina cup.

2.2.5. Microscopy

Visual inspection of LDH modified fibers before and after TG analysis, was done with a Leo Gemini 1530 field emission scanning electron microscope that was equipped with In-Lens detector (LEO Electron Microscopy Ltd., Oberkochen, Germany). Modified samples were coated with carbon in Temcarb TB500 sputter coater (Emscope Laboratories, Ashford, UK). Optimum accelerating voltage for modified samples was 2.70 kV and 15.0 kV for the incinerated samples. The working distances were, respectively, 5–6 mm and 13–14 mm.

For TEM experimentation, the epoxy resin-embedded sample blocks were sectioned with an ultra-microtome (Leica EM UC7) equipped with a diamond knife. Sections of 200 nm in thickness were picked on 600 hexagonal mesh copper grids. Ultra-thin sections were examined with an FEI Tecnai 12 transmission electron microscope at a 120-kV accelerating voltage.

2.2.6. Microrobotic Platform

A microrobotic platform, the mechanics and the user interface of which were designed and developed at Tampere University of Technology, was implemented to perform the compliance experiments for individual pulp fibers. In addition, a MATLAB code was utilized to calculate the compliance from the raw data. Experimental results were tested against the null hypothesis. The *t*-test was applied to calculate the result significance. Ten fibers from each batch were forced to flex five times in our experiments, and the averaged compliances were calculated from the force sensor data. The platform and its application for pulp fiber characterization is explained by Saketi *et al.* [30]. In the method, a pulp fiber is gripped from both of its ends by two microgrippers (Figure 1). A force sensor is then positioned at the midpoint of the fiber's free span. The applied force (F) is measured five times by setting the maximum deflection limit (Y_{max}) in meters (m) according to the fibers linear elastic range. The extent of deflection is fixed in all experiments. For calculating the compliance, the fiber was considered as a rectangular beam with both of its ends fixed in position. It is generally known that F in this particular

case is related to Y_{max} according to Equation (1).

$$Y_{max} = \frac{F \cdot L^3}{192 \cdot E \cdot I} \tag{1}$$

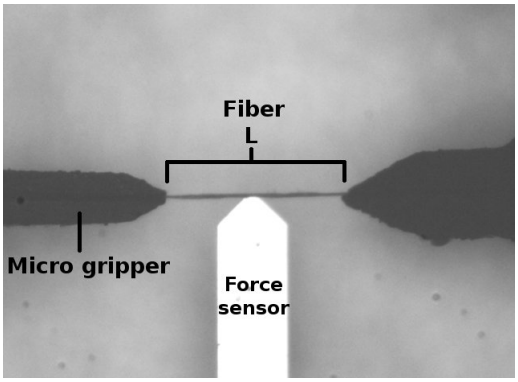

Figure 1. An image of the setup in the microrobotic platform for compliance measurement.

In the given equation, L is the free length (m) of the beam, E is its young modulus (N m^{-2}), and, I is its moment of inertia (kg $\cdot$ m^2). The compliance of the beam is defined as follows.

$$\frac{1}{k} = \frac{1}{E \cdot I} \tag{2}$$

The k is the stiffness of the body. The Equation (1) can then be rewritten according to Equation (3), from which the k^{-1} can be calculated.

$$Y_{max} = \frac{F \cdot L^3}{192 \cdot k} \tag{3}$$

2.2.7. Capillary Viscometry

Intrinsic viscosity was determined with capillary viscometer to address the possible cellulose polymer degradation induced by LDH synthesis. The apparatus and applied method is described in the standard ISO/FDIS 5351:2009(E). The viscosity is determined by recording the time for the CED solution that contains dissolved pulp fibers to flow through a pre-determined volume in a 0.8 ± 0.05 mm capillary-tube viscometer at 25 °C (298 K). Calibration of the capillary-tube viscometer was performed with 65% glycerol solution that has a known viscosity (10 mPa $\cdot$ s) at the given temperature. The CED solution was controlled by comparing the efflux time ratio for diluted CED (0.5 M) to distilled water. The value should lie in between 1.27 and 1.29 to assure the freshness of CED solution. We found the value to be 1.284. Viscometer constant was then measured with two capillary-tube viscometers and calculated according to Equation (4). The limiting viscosity number for each sample was calculated from Equation (5) by using the tabulated values set according to [31] for viscosity ratio as defined in Equation (6). Measurements were repeated as many times as required to reach 2% relative standard deviation.

$$h = \frac{t_c}{t_v t_s} \tag{4}$$

The t_c is the time (s) for the glycerol to flow through calibration viscometer with diameter of 0.58 ± 0.02 mm, t_v is the time for glycerol to efflux through the capillar-tube viscometer that is used for the sample solutions, and, t_s is the time for 0.5 M CED solution to efflux through the calibration viscometer.

$$\eta_{sample} = \frac{T}{\rho} \tag{5}$$

The T is the tabulated empirical value for a given sample with efflux time t, and, ρ is the mass concentration ($g \cdot mL^{-1}$) of the sample.

$$\eta_{ratio} = \frac{\eta}{\eta_0} = h \cdot t \tag{6}$$

The t is the time (s) for the test solution to pass through the capillary viscometer.

2.2.8. Adsorption Isotherms

An adsorption isotherm with MB was conducted at 298 K (25 °C) as described by Fardim *et al.* [32]. Fibers with oven dry mass of 102 ± 2 mg were suspended in 3 mL of deionized water for 30 min. Methylene blue solution ($c = 400$ μM) was then added into the sludge and the sorption was allowed to proceed at 298 K (25 °C) for 15 min under gentle shaking. The MB solution was buffered with 600 μM barbital to pH 8.2. Samples were filtrated through a glass fiber filter under reduced pressure after the sorption process. Filtrate was diluted 20 fold in 20 mL volumetric flask. The method was also applied with MY adsorption experiments. Approximately 30 mg of pulp fibers were allowed to soak and react with the adsorbate as in MB sorption experiment. Initial concentration of MY solution was 49 ± 1 μM. The adsorption isotherms were constructed by using different volumes of adsorbate solution. Ionic strength was controlled with KCl and set to 1 mM. Concentration of an equilibrium filtrate was recorded with UV-Vis instrument. Wavelength maxima for MB was 664 nm and 436 nm for MY.

Adsorption isotherms were evaluated with the Langmuir model defined in Equation (7), where $[i]_{eq}$ is the equilibrium concentration of the adsorbate and K is the equilibrium constant. Noting that the surface coverage (θ) can be expressed as a fraction of adsorbed substances at equilibrium (a_{eq}) to maximum adsorption (n), the equation can be rearranged according to Equation (8). The correlation factor of fitted straight line for each sample was greater than 99%.

$$\theta = \frac{K \cdot [i]_{eq}}{1 + K \cdot [i]_{eq}} \tag{7}$$

$$\frac{a_{eq}}{n} = \frac{K \cdot [i]_{eq}}{1 + K \cdot [i]_{eq}} \Leftrightarrow \frac{[i]_{eq}}{a_{eq}} = \frac{1}{nK} + \frac{[i]_{eq}}{n} \tag{8}$$

3. Results and Discussion

3.1. LDH Synthesis

3.1.1. X-Ray Diffractometry

The XRD difraction patterns for neat LDH and for a commercial reference (HT) are shown in Figure 2 and the data is tabulated in Table 1. For each lattice diffractions the full width half maximum (FWHM) values and basal spacing (*l*) increased in the order of LDH-U < LDH-C < HT < LDH-OH. Particle size should follow the reverse order. Asymmetric line broadening of 012 and 015 reflections in LDH-OH was also noticed with highest calculated basal spacing *l*. One possibility is that LDH-OH is a randomly intergrown rhombohedral structure as described by Evans and Slade [33]. Interstatification of hydroxyl ions has most likely occured, but also, NO_3^- may have entered into the gallery due to statistical reasons because metal nitrates were used in synthesis. Experimental results may also arise from micro strain induced lattice distortions and from the inclusion of water molecules [33]. In any case, the LDH structures can be assigned as one layer polytypes.

Table 1. The characteristic diffraction angles (2θ), fitted lattice parameters ($a = b, c$) assuming R-3m space group symmetry, basal spacing (l), full width half maximum values (FWHM), relative peak hight (RPH) and signal to noise ratio (S/N) are presented for each LDH sample. The generally known Miller indices (*hkl*) for each recorded lattice spacings in LDH, that are stacked in rhombohedral sequence via octahedral arrangement of OH groups, are: 003, 006, 012 and 015.

Sample	**2θ**	$a = b$	c	l	**FWHM**	**RPH**	**S/N**
	deg.	Å	Å	Å	**deg.**	**%**	
HT	11.68	3.10	22.73	7.58	0.522	100	360
	23.28				0.781	29	105
	34.90				0.763	14	50
	39.44				0.613	14	50
LDH-U	11.85	3.04	22.45	7.48	0.266	100	280
	23.71				0.309	33	93
	35.04				0.257	11	31
	39.70				0.297	11	30
LDH-C	11.75	3.08	22.61	7.54	0.459	100	47
	23.53				0.426	55	26
	34.60				1.000	32	15
	39.52				0.631	21	10
LDH-OH	11.71	3.09	22.77	7.59	0.893	100	37
	23.44				1.125	43	16
	34.63				1.302	35	13
	38.68				1.830	14	5

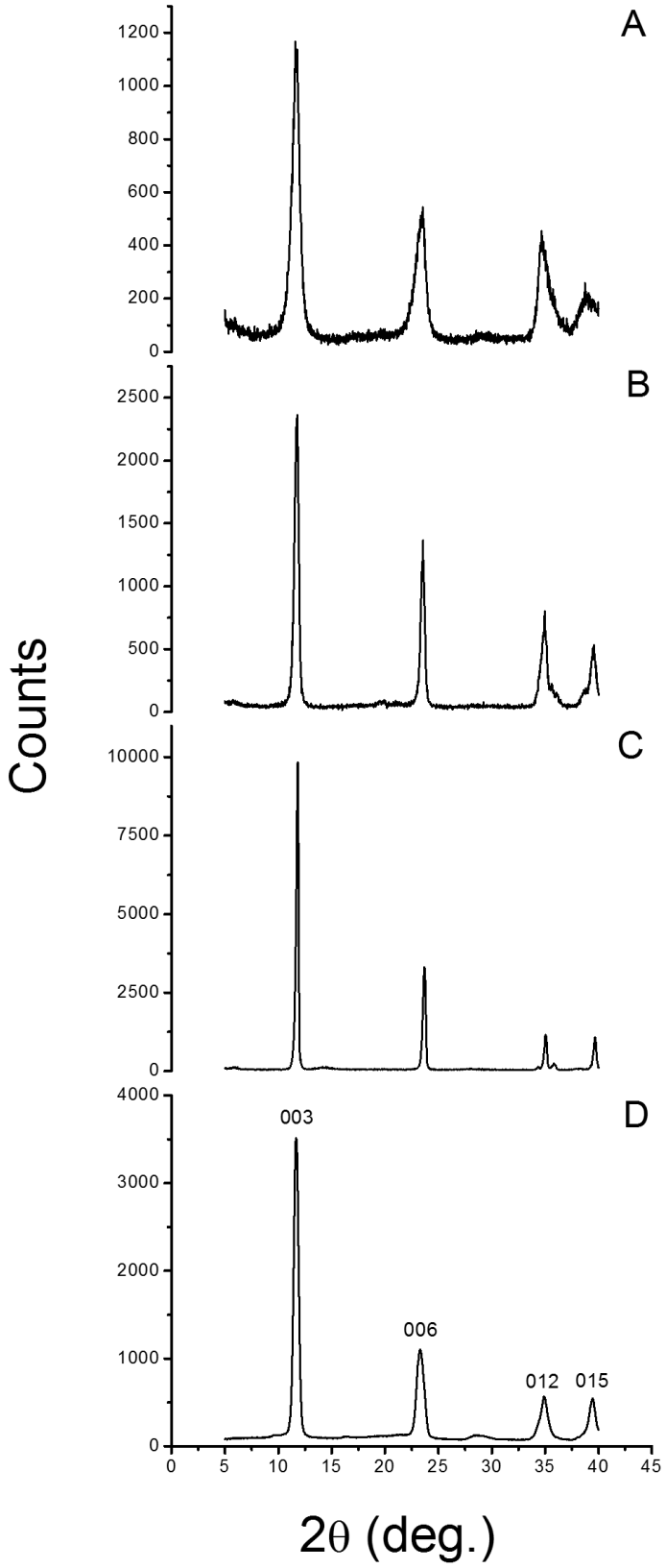

Figure 2. The XRD signals for different LDH particles are presented. (**A**) LDH-OH; (**B**) LDH-C; (**C**) LDH-U and (**D**) commercial HT .

3.1.2. Thermogravimetry

The TG and differential thermal analysis (DTA) from the neat LDH particles are shown in Figure 3. Thermogravimetric response of a typical LDH can be divided into three sections [34] in the given temperature range where LDH structure can still be reconstructed in aqueous environment. First is the loss of adsorbed water and partial dehydroxylation until T = 523 K (250 °C). Depending on the LDH structure, some interlayer water may be lost already at this stage [35]. The accompanying loss of chemically bound water from the LDH galleries appears in between 548 and 623 K (275–350 °C). Some carbonates and hydroxyls are removed as well. It has been proposed that the dehydroxylation of Al-OH takes place some 30 K before Mg-OH that is accompanyed by decarbonation [35]. Crystal lattice reordering will, therefore, begin to take place in this temperature range. The third endotherm starting from around 650 K (377 °C) is associated with significant loss of CO_2 and OH during which the layered structure collapses and oxolation to M^{II}-O-M^{III} occurs.

The first endothermic signal in LDH-OH is spread over a large temperature range until 505 K (232 °C) during which 15.2% from weight is lost (Figure 3A1,2). Most of the weight reduction comes from loss of water but some hydroxyls may be removed as well. Since the water is removed gradually from the LDH structure without a sharp endotherm except at the very end of the temperature range, an amorphous structure can be envisaged. The separation of the two main endothermic peaks was smallest in LDH-OH sample ($\Delta T = 160$ K) leaving the endotherms at the middle temperature range, denoting loss of chemically bound water, carbonate and hydroxyl, almost invisible. A subtle shoulder in TG is found at 590 K (317 °C). The remaining temperature range is characterized with 28.6% reduction in weight. The LDH-OH seem to loose majority of hydroxyls and carbonates in reactions where the separation in between dehydroxylation of Al-OH and Mg-OH and decarbonation processes can not be made.

For LDH-C the first temperature range proceeds up to 513 K (240 °C) with 14% weight reduction (Figure 3B1,2). An exothermic signal at 555 K (282 °C) was found in the second temperature range that is characterized by loss of chemically bound water, carbonates and hydroxyls from Al-OH. It is not clear from which phenomenon the exotherm originates exactly. Detected endothermic shoulder at around 595 K (322 °C) may arise from dehydroxylation of Mg-OH and loss of carbonate. Weight was reduced by 13.4%. Concomitant loss of residual carbonate is denoted as a last endotherm at 673 K (400 °C) with 15.8% weight loss continuing until 873 K (600 °C).

Thermogravimetry of LDH-U has three distinctive endotherms in each temperature range already explained (Figure 3C1,2). The endothermic signals are located at 468 K (195 °C), 558 K (285 °C) and 698 K (425 °C). Accompanying weight losses are 14.1%, 7.4% and 19.2% respectively. We propose that a loss of interlayer water and dehydroxylation of Al-OH occurs at 558 K (285 °C) while dehydroxylation of Mg-OH and loss of carbonates are simultaneous processes at 698 K (425 °C).

It should be noted also, when comparing TG from HT and LDH-C, that competing reactions may take place in temperature range of $550-570$ K ($277-297$ °C). The reference particles seem to express a small endotherm at 564 K (291 °C) while concomitant weight loss is 11.7% (Figure 3D). Also, the endothermic signal that is assigned for significant loss of CO_2 and OH moves further to higher temperatures in the order *lss* < *hss* < HT $\simeq$ *Uhyd* thus pointing towards thermodynamic stability of the carbonates in the

LDH gallery. Furthermore, LDH-OH may have significant amount of interstratified NO_3^- in its structure that lowers the apparent thermodynamic stability.

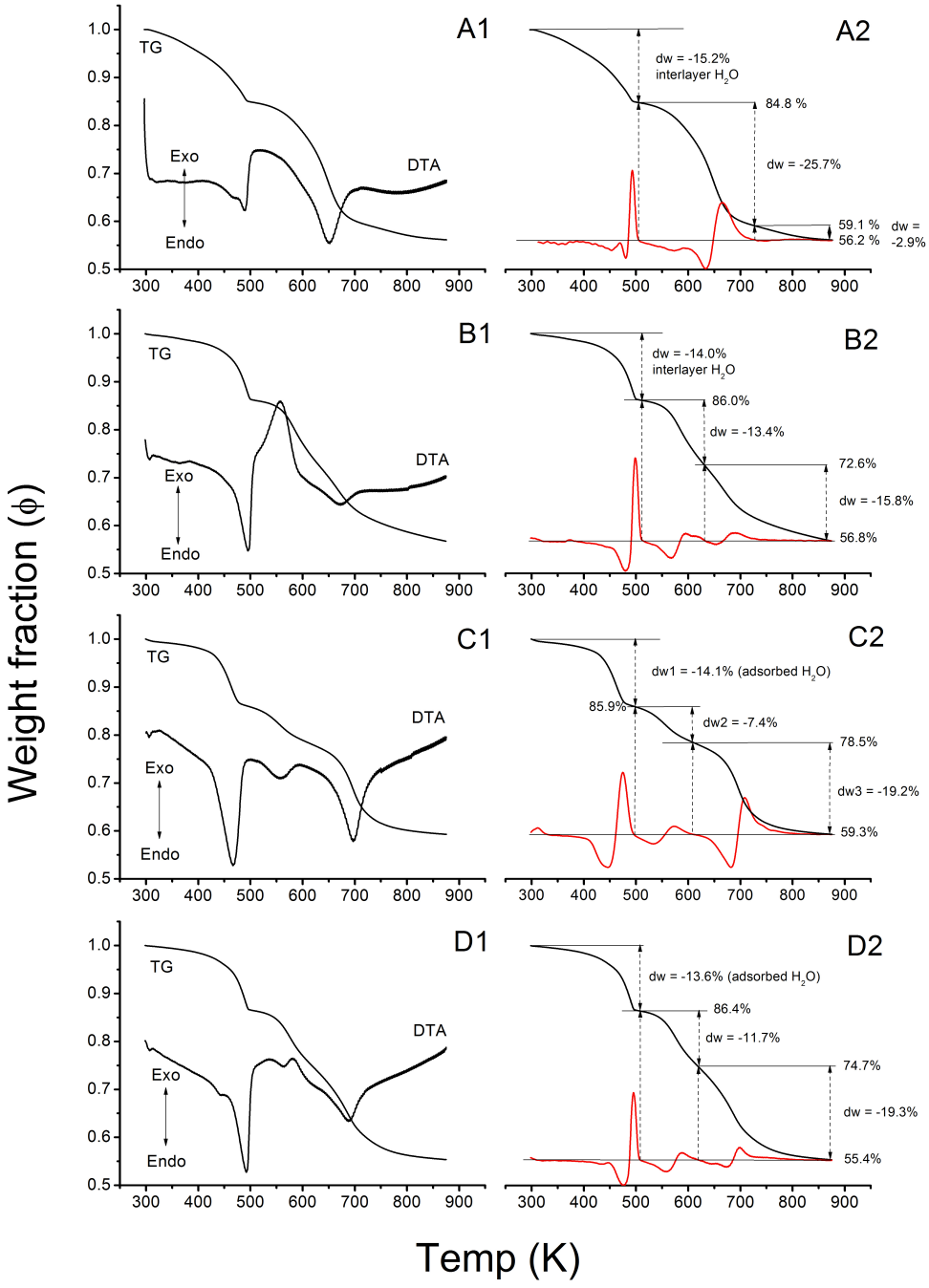

Figure 3. The weight fraction (ϕ) for LDH-OH (**A**); LDH-C (**B**) and LDH-U (**C**) particles is plotted as a function of temperature (T); Commercial HT (**D**) is shown as a reference. Endo- and exotherms are presented in (**A**1–**D**1). Rationale for weight reductions from experimental values are shown in (**A**2–**D**2). Second derivative of TG is shown in red.

3.1.3. ATR-FTIR

The area of group frequencies above 2750 cm^{-1} shows similarities between HT, LDH-OH and LDH-C (Figure 4A). Two sharp peaks at 2917 and 2850 cm^{-1} vibration frequencies were found from HT, LDH-C and, albeit as extremely weak shoulders that are not resolved in the given figures, from LDH-OH. For LDH-U, a broad asymmetric signal was observed instead, but it may be that the sharp signals are embedded underneath. The shoulder at around 3000 cm^{-1} is attributed to hydrogen bond stretching between carbonate and water within the LDH gallery [36].

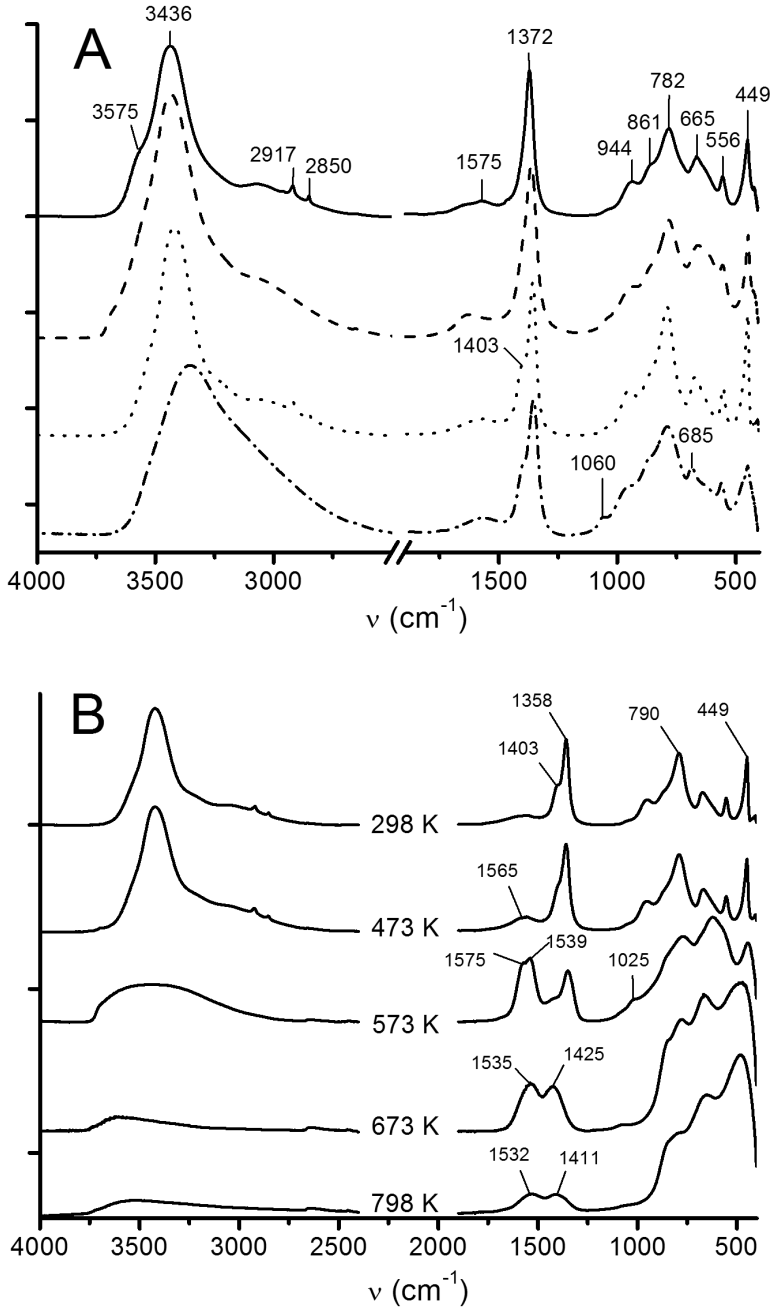

Figure 4. ATR-FTIR spectra of (**A**) different LDH particles with commercial reference (HT); and (**B**) after thermal decomposition of LDH-C particles. HT (–), LDH-OH (- - -), LDH-C (· · ·) and LDH-U (– · –).

The asymmetric stretching vibrations (ν_3) from CO_3^{2-} in the LDH gallery were observed at 1372–1358 cm^{-1} (Figure 4A). Out-of-plane bending vibration (ν_2) appears at about 860 cm^{-1} and in-plane bending (ν_4) at 665 cm^{-1}. A shoulder in ν_3 vibration at 1403 cm^{-1} was found in LDH-C and LDH-U samples. The symmetric stretching vibration (ν_1) of CO_3^{2-} at 1060 cm^{-1} is IR inactive in the free ion, but may become visible if the space symmetry is changed [33,37]. This symmetry change is often related to the splitting of ν_3 into two, as planar CO_3^{2-} D_{3h} becomes pyramidal C_{2v} or C_s [33,36,38]. The split parameter of about 30–60 cm^{-1} in ν_3 is proposed to arise due to a change in the force constant of hydrogen bonds between the CO_3^{2-} and OH groups in the interlayer lamina [33]. Differences in site and point symmetry-induced vibrational frequencies of carbonate in different minerals are well explained by Adler and Kerr [39]. The broad and small peak at around 1575 cm^{-1} arises from coordinated carbonate ions ([37], p. 284). Water may interfere at 1650 cm^{-1}, at least in the LDH-OH sample. It can be established then that in LDH-C and LDH-U, the carbonate occupies two different space symmetries owing to the splitting of ν_3, while all samples have a broad peak at around 1575 cm^{-1}, indicating both coordinated and free carbonate ions. It should be noted here, likewise, that the chosen precursors for LDH may obscure LDH-OH interpretation in that carbonate is replaced partially by nitrate ions. The vibrations for NO_3^- are close to CO_3^{2-}, so that differentiation is difficult.

The FTIR signals show typical changes upon thermal treatment of LDH, as described, for example, by Ray *et al.* [40] (Figure 4B). First of all, the LDH-C is stable up to 473 K (200 °C). Splitting of the ν_3 vibration of coordinated carbonate into two new bands (1539 cm^{-1} and 1575 cm^{-1}) is detected at 573 K (300 °C). The relative intensity of ν_3 at 1358 cm^{-1} is decreasing at the same time, while the splitting remains. The difference for ν_3 in coordinated and free ions is 170–175 cm^{-1}, depending on the synthesis route. Therefore, as water and hydroxyl ions are being lost from the LDH structure, the carbonate becomes coordinated and restricted by the symmetry at the same time. The stretch vibrations from coordinated CO_3^{2-} should appear also around 800–700 cm^{-1}, but this area coincides with M-O stretch and OH deformation vibrations, and thus, cannot be used in detection. It should be noted here that owing to the basic principles of vibration spectra, the so-called polarization power of the cations in LDH must influence the hydrogen bonding strength of the associated OH^- in octahedral sites that, in turn, will determine the difference in observed vibrational spectra between the coordinated carbonate and the free ion. Carbonate that is coordinated as a bidentate ligand should have greater separation of the vibrational adsorption band to the free ion than a monodentate ligand has. Therefore, the carbonate in each synthesized LDH particle occupies a more or less similar site symmetry, either in uni-, or bi-dentate, or both, but we expect the carbonate to be a bidentate bridging ligand at 573 K (300 °C).

The area below 950 cm^{-1} changes significantly from 473–573 K (200–300 °C) and again from 573–673 K (300–400 °C). The second and third endotherms detected in TG are located in these regions. Group vibrations for OH were also changing. The phenomenon is interpreted as a collapse of a layered structure due to loss of carbonate and the formation of mixed metal M^{II}-O-M^{III} bridges upon dehydroxylation [40]. The asymmetric ν_3 vibrations from CO_3^{2-} changes, so that the splitting disappears and the difference between coordinated and free ion reduces to 100–120 cm^{-1}). The carbonate signal represent more free-like ion and possibly monodentate coordination at 673 K (400 °C). The reduction in the bonding strength of carbonate to $M^{II/III}$-O with a more free ion character is also expected. It is important to note that in the spectrogram of LDH-OH particles, a shoulder appeared at 1355 cm^{-1} after

heating the sample up to 673 K (400 °C) (see supporting Figure S1). This vibration fits rather well for the free NO_3^- ion ([37], p. 285).

3.2. Mineralization and Coating of Pulp Fibers

The reference pulp that was used in all experiments was fully bleached Kraft fibers from pine. The Kappa number of such pulps is usually less than 4 even after moderate bleaching stages, and, it is affected by residual lignin, hexenuronic acids as well as other carbohydrates that contain sp^2 hybridized carbons with double bonds ([41], p. 769). The residual lignin content in delignified and bleached softwood fibers after Kraft process is very low and average cellulose and hemicelluloses content are in the range of 85% and 15% respectively ([41], p. 1013).

3.2.1. Microscopy

SEM images (Figure 5A1–C1) confirmed that the hydrolytically synthesised particles with pulp fibers appeared similar to typical LDH that has been synthesised by other authors in absence of template structures such as fibres [26,42,43]. The hexagonal shape was especially clear from clay sized particles (insets in Figure 5C1,2). All synthesis routes produced uniformly distributed particles on fibers external surfaces. Also, the particles size followed the proposed order from XRD. The LDH from *lss* and *hss* solutions were $\leq$200 nm while those from *Uhyd* were approximately 2–5 µm in diameter. The SEM images taken after TG analysis indicated that the fibers were acting as templates for LDH (Figure 5A2,B2 and C2).

Surprisingly, effective particle nucleation within the S2 cell wall was discovered with TEM after *Uhyd* synthesis (Figure 6A). We concluded that the LDH particles were not spread over the imaged area by the diamond blade during ultra-thin sectioning of epoxy moulded specimen as there were no similarly distributed particles to be seen anywhere over the polymer matrix apart from some agglomerated bundles that were found in ultra thin sections from *hss* and *lss* treated fibers (Figure 6B,C). We expect that the particle nucleation within the fiber wall was inhibited in *hss* system due to rapid pH change that signify rapid olation of ions prior to crystall growth. In *lss* route, on the other hand, the fibres were completely saturated and swollen as the pH was kept above 9 throughout the reaction. The nucleation kinetics prevented, however, the diffusion of Mg^{2+} and Al^{3+} ions into the cell wall structure albeit in some TEM images small amount of nanoparticles were observed in S2 layer. Colloidal particles can therefore migrate into the fiber wall to some extent. Swelling and nucleation in *Uhyd* system was expected to be slow and fully controlled by the rate of urea hydrolysis.

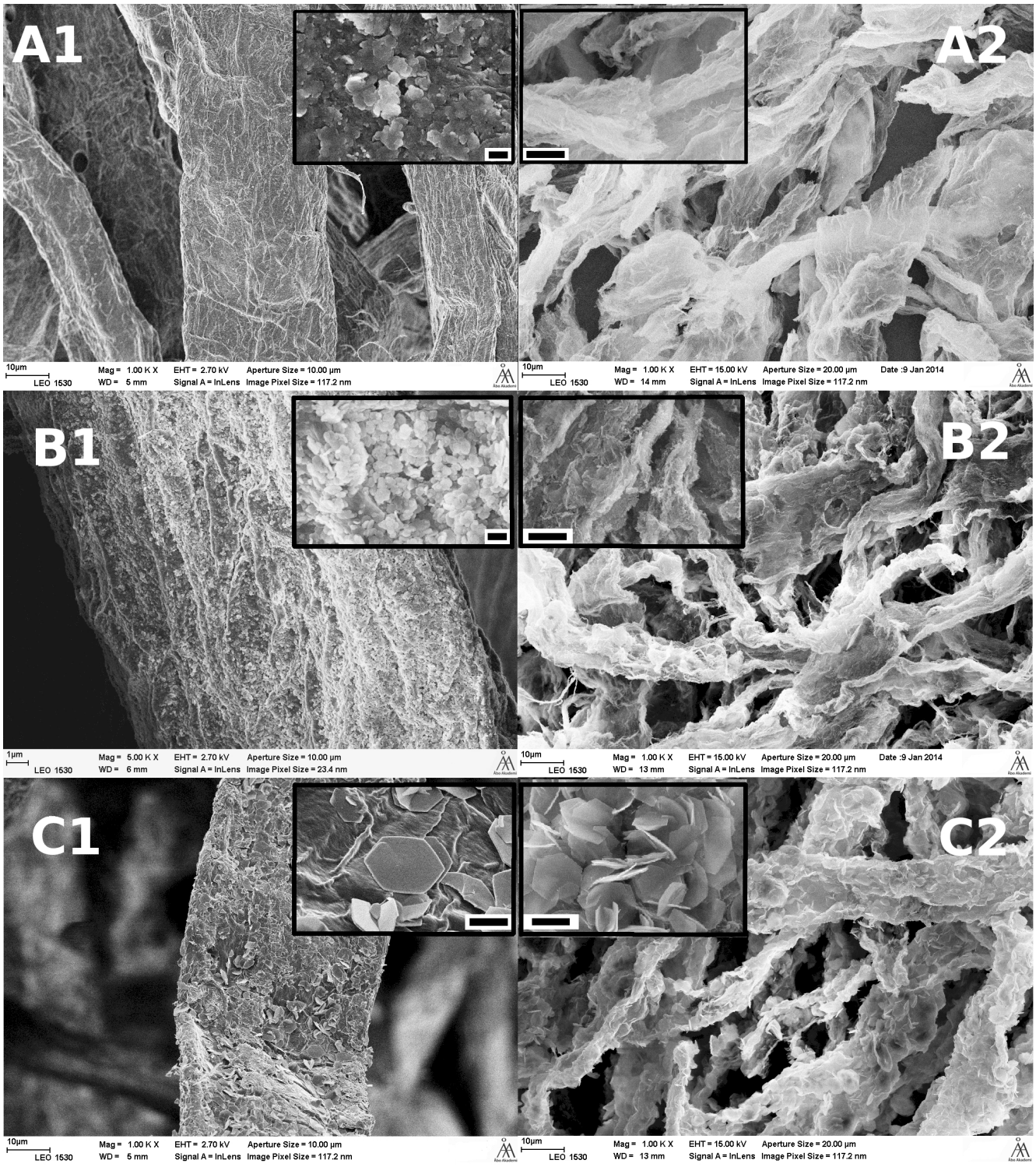

Figure 5. SEM images of (**A**) *lss* synthesised; (**B**) *hss* synthesised and (**C**) *Uhyd* synthesised fibers before (1) and after (2) TG analysis. The scale bar in the insets are (**A**1 and **B**1) 200 nm and (**C**1–**C**2) 2.0 µm. The width of a collapsed wood fiber before incineration was approximately 30–40 µm.

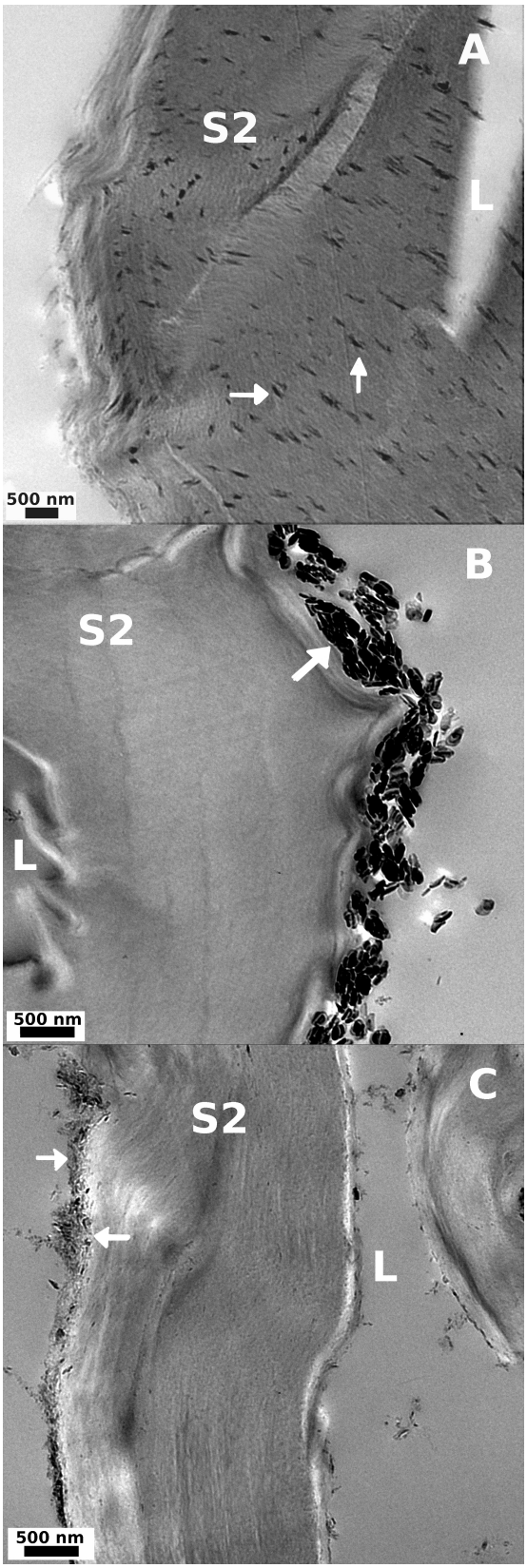

Figure 6. TEM images from transverse cut (**A**) *Uhyd* and (**B**) *hss*; and (**C**) longitudinal cut *lss* treated fibers. The particle size follows the order LDH-U > LDH-C > LDH-OH. Fiber lumen (L) and cell wall (S2) are visible in all samples. LDH is marked with arrows.

The reason for the patterned and apparently lamellar distribution of nanoparticles in S2 cell wall after *Uhyd* synthesis is unknown, but, we assume that the existence of carboxyl functionalities in a form of hexenuronic and 4-*O*-glucuronic acids plays an important role (*c.f.* Section 3.2.6). Pore size will undoubtedly affect to migration of nano-particles and nucleation within the cell wall structure as well. Depending on the chosen pulping technique the pore size distribution can extend to meso and macro range up to 30 nm [44,45]. There is also evidence that the swollen fibres have even larger pores up to 100 nm in size [46]. The pore size and depth in fibers transverse direction was not addressed. It is also known that fiber swelling is somewhat reduced in a solvent with high ionic strength [47]. Considering the differences in between the *hss* and *Uhyd* synthesis routes, the electrostatic driven diffusion of Mg^{2+} and Al^{3+} ions into fiber wall must be rapid and occur at elevated pH preceding particle formation. The rationale goes as follows. First of all, in *hss* system the fiber swelling lacks behind pH change whereas in *Uhyd* the extent of swelling and pH increase are approximately concomittant processes. In alkaline environment the fiber swelling gradually advances with the aid of increased temperature. Increasing the activity of hydroxyls will draw cations into the fiber wall [48]. Increase in ionic strength within the cell wall will ultimately cause the swelling as water enters into the structure due to osmotic pressure that, at some pH, will overcome the cohesion of the lamellar structure in radial direction of the fibre and change its structure [45,49] allowing more of the bound charged groups to be available for cations to interact. It is known that the pK_a for uronic acid in pulp is approximately 3.1–3.3 [50]. The pH for a solution in which the pulp fibers were soaked prior to hydrothermal treatment containing Mg^{2+} and Al^{3+} ions was 3.7 at which, considering the pK_a, some 60%–75% of uronic acids are deprotonated. The interaction and distribution of different metal ions with apparent equilibrium constants in between pulp fibres and bulk solution at diffirent pH have been addressed by many authors [51–53]. It is therefore possible that the water molecules in the S2 cell wall are partially exchanged to urea, and, at the hydrolysis temperature, ammonia and carbonate induce local pH increase within the fiber wall facilitating the diffusion of ions into the fiber structure according to Donnan equilibrium model, and, ultimatly leading to formation of $Mg(OH)_2$ and $Al(OH)_3$ and LDH. The validitiy of Donnan model in context of pulp fibers is discussed in several papers [54–56]. The consensus is that Donnan model is satisfactory at moderate pH range (3–6) where precipitation of metal hydroxides do not occur and ion interactions with semi-permeable membrane, *i.e.*, fibre cell wall, are non-specific [57–59].

We cannot rule out at this point the possibility that the nucleation within the S2 cell wall produces other than LDH particles also. It is evident from TEM and SEM images, however, that all synthesis routes coagulate LDH particles effectively onto the fiber surface. Particle size from *hss* system is observed to be close to the one found in SEM images. The *lss* synthesis route produced particles with size in the nano regime (<100 nm). Significant densification of pulp fibers was expected because of the mineralization action of *Uhyd* treatment (*c.f.* Section 3.2.5).

3.2.2. Thermogravimetry

Changes in weight were recorded after thermal stabilization at 473 K (200 °C) (*c.f.* Section 2.2.4). The point where the rate of mass change exceeded $-0.025\ \mathrm{mg \cdot K^{-1}}$ was chosen as the onset temperature (Figure 7A inset). Onset temperature for the reference pulp was 497 ± 3 K (224 ± 3 °C) while the LDH modified pulp samples showed insulating effect up to 519 K (246 °C). Regardless of the onset

temperature, the first combustion reaction levelled out in each sample at 620 K (347 °C). The mass loss rate appeared higher for *lss* and *Uhyd* samples (Figure 7A).

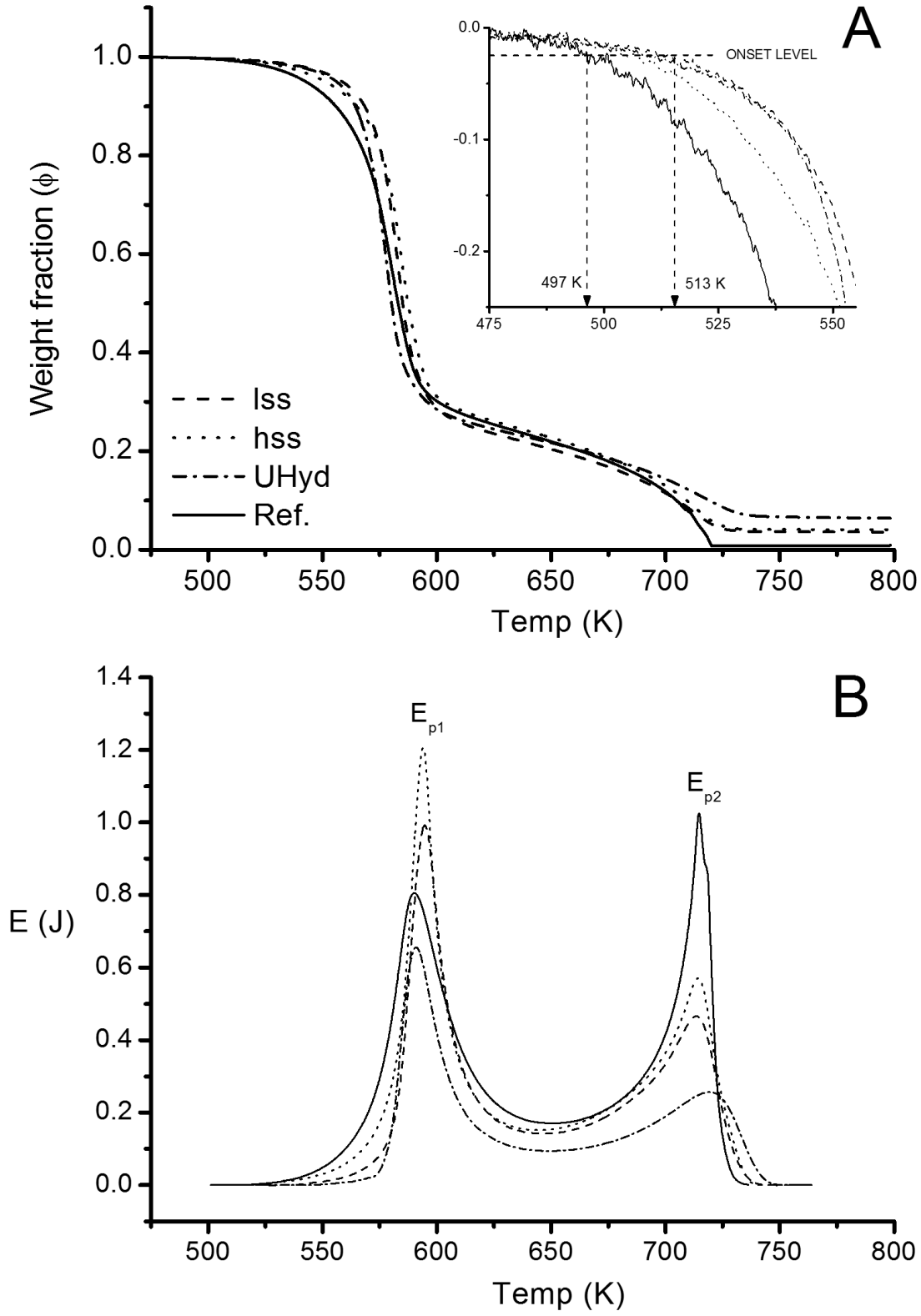

Figure 7. (**A**) The thermograms and onset temperature analysis (inset) for oxidative combustion of fully bleached Kraft pulp fibres from Pine with LDH (*lss*, *hss*, *Uhyd*) and without (Reference) (**A**); and released energy at a given temperature (**B**) are presented.

Pulp fiber degradation occurred in two phases with the chosen set up. First mass loss at around 498–620 K (225–347 °C) comprised approximately 77% from the dry weight and produces oxidised cellulose and carbon containing char. Second mass loss occurred at 673–748 K (400–475 °C). Combustion is characterized with CO_2, CO and CH_4 evolution from hemicelluloses and cellulose [60]. The main gaseous component, CO_2, is released in two phases. For hemicellulose (xylan) the release occurs at 518 and 623 K (245 °C and 350 °C) while for cellulose (micro crystalline) the peaks are at 593 and 748 K (320 °C and 475 °C) [61]. The results were obtained under airflow.

The average residual mass from *hss*, *lss* and *Uhyd* pulps were 3.6%, 4.1% and 6.5% respectively (Figure 7A). Standard deviation for the residual mass in each pulp was 2%. The standard deviation increased with the amount of LDH in pulp, probably due to small sample weight that was required for TG experiments. Fully bleached Kraft reference pulp fibers contained approximately $0.8\% \pm 0.2\%$ of ash. Using the weight loss data from TG analysis of pristine LDH particles (Figure 3) it is possible to calculate the initial weight fraction of LDH (Ψ°_{LDH}) for each pulp samples. The values are given in Table 2. The apparent relative weight increase of organic substances (Ψ^{473}_{org}) was due to chosen reference point at 473 K (200 °C). LDH had lost approximately 14%–15% in a form of water (Figure 3) at that temperature. The standard deviation of detected weight fraction after the first exotherm was approximately 2.5% regardless of the sample. Hence, the fraction ($\Delta\Psi$) was averaged over the entire sample set.

Table 2. The calculated weight fraction of organic material (org) and LDH particles in LDH containing fibers are presented at three different temperatures: initial stage at 298 K (25 °C) (Ψ°_{org} and Ψ°_{LDH}), after conditioning at 473 K (200 °C) (Ψ^{473}_{org} and Ψ^{473}_{LDH}) and prior to the second exotherm at 643 K (370 °C) (Ψ^{643}_{org} and Ψ^{643}_{LDH}). Relative average total mass loss of material during the first exotherm ($\Delta\Psi$) and relative total mass loss of LDH in combustion ($\Delta\Psi_{LDH}$) are presented as well. Material specific unit energies for both corresponding exotherms (E_{p1} and E_{p2} *cf.* Figure 7B) with the total exothermic energy ΣE and the LDH reduced energy E^0_{p1} are included in the table.

Sample	Ψ°_{org}	Ψ°_{LDH}	Ψ^{473}_{org}	Ψ^{473}_{LDH}	Ψ^{643}_{org}	Ψ^{643}_{LDH}	$\Delta\Psi$	$\Delta\Psi_{LDH}$	E_{P1}	E^0_{P1}	E_{P2}	ΣE
	%								$kJ \cdot g^{-1}$			
Reference	100	–	100	–	100	–	78	–	3.9	3.9	11.7	15.6
lss	95.0	5.0	95.8	4.2	84.5	15.5	78	43.8	2.6	3.1	7.3	9.9
hss	94.2	5.8	95.0	5.0	81.8	18.2	78	43.4	3.0	3.7	7.6	10.6
Uhyd	90.4	9.7	91.7	8.3	67.0	33.0	78	40.8	1.7	2.5	4.3	5.0

In order to relate the exothermic signals from DTA to the combustion enthalpies ($\Delta_c U$), the instrument was calibrated with high purity Pb and Zn standards. Fusion enthalpies were chosen from a critical review by Stølen and Grønvold [62]. Corresponding experimental properties are given in Table 3. Since the thermogravimetric data for modified pulp samples spans over a range of 520–740 K (247–467 °C), the calculated unit energies from the standards were fitted with a linear function. The parameters for the linear fit ($y = a + bx$) were: $a = 0.039$ J $\cdot$ K^{-2} and $b = 3.8 \cdot 10^{-4}$ J $\cdot$ K^{-3}. Exotherms from modified pulp fibers are shown in Figure 7B. The onset temperature for exothermic signals were determined from the first derivative of DTA curve. It should be noted that the recorded

exo- and endotherms are influenced by the temperature ramp, carrier gas and its flow rate, initial material weight and its density, and, instrument design to some extent. Accurate enthalpies are therefore difficult to calculate in such open system. However, the calculated combustion enthalpy (ΣE) for the reference fibers was reasonably close to the ones found in the literature [63,64]. The ΣE was clearly reduced by the LDH especially after *Uhyd* synthesis (Table 2). Cellulosic polymers were expected to interact with LDH at the particle-polymer interphase. The calculated enthalpies related to the exotherm E_{p1} (Figure 7B and Table 2) suggests, at first, that LDH influence is size dependent and also affected by the location of the particles. For example, *hss* has higher E_{p1} than *lss*. However, when E_{p1} is corrected by removing the effect of LDH (E^0_{p1}) a perfect correlation ($R \simeq 1$) in between the enthalpy and weight corrected intrinsic viscosity of the LDH containing fibers is found (*c.f.* Table 4). The paramters for a linear function ($y = a + bx$) were: $a = 526.5\ \mathrm{mL \cdot g^{-1}}$ and $b = 95.0 \cdot 10^{-3}\ \mathrm{mL \cdot J^{-1}}$. Furthermore the diffence in E_{p1} and E^0_{p1} provide means for evaluating the effect of LDH. Enthalpy reduction in each case was substantial but the difference only from 0.5 to 0.8 kJ g^{-1} corresponding to 17%–25% reduction from the expected 3.9 kJ·g^{-1}. increasing in order *lss* < *hss* < *Uhyd*. Second exotherm (E_{p2}) correlated reasonably well with the residual LDH content (Ψ^{643}_{LDH}).

Table 3. The calibration standards with corresponding physical properties and experimental unit energies ($\Delta_c U_{unit}$) are presented. The $\Delta_{fus}H_m$ was acquired from Stølen and Grønvold [62] and the litterature values for the melting point onset (mp.) from Ditmars (Zn) and Zahra & Zahra (Pb) [65,66].

Standard	**M**	$\boldsymbol{\Delta_{fus}H_m}$	**mp. (Litterature Value)**	**n**	$\boldsymbol{E_{tot}}$	$\boldsymbol{\Delta_c U_{unit}}$
	g·mol^{-1}	**J·mol^{-1}**	**K**	**µmol**	***J***	**J·K^{-2}**
Pb	207.20	4765 ± 11	600.13 (600.61)	243	1.158	0.2699
Zn	65.39	7103 ± 31	692.25 (692.68)	275	1.951	0.3054

3.2.3. ATR-FTIR

The combustion induced spectral changes are depicted in Figure 8A–E. Isothermal conditioning at 473 K (200 °C) removes all absorbed water from the pulp fibers. Fiber degradation was not observed at that temperature in the given timeframe. LDH is apparent only in *hss*, due to thick particle layer on the fiber surface, as seen in TEM images, on this particular sample (Figure 8A). Material degradation occurred in each sample at 573 K (300 °C) as the C=O stretching vibration appeared at 1726 cm^{-1} (Figure 8B). After initial combustion process at 613 K (340 °C) the LDH containing fibers expressed various absorption vibrations from ketones and acids in the region of 1750–1400 cm^{-1}. Some pyranose ring vibrations at 1400–1020 cm^{-1} were still visible in LDH containing samples. Approximately 70% of the material is lost at that temperature according to TG wherefore the characteristic M^{II}-O-M^{III} and M-O stretch vibrations from LDH becomes apparent below 900 cm^{-1} as well (Figure 8C). It should be noted that the ν_3 vibrations from carbonate are located close to the carboxylic acid vibrations around 1600 cm^{-1} and 1410 cm^{-1}.

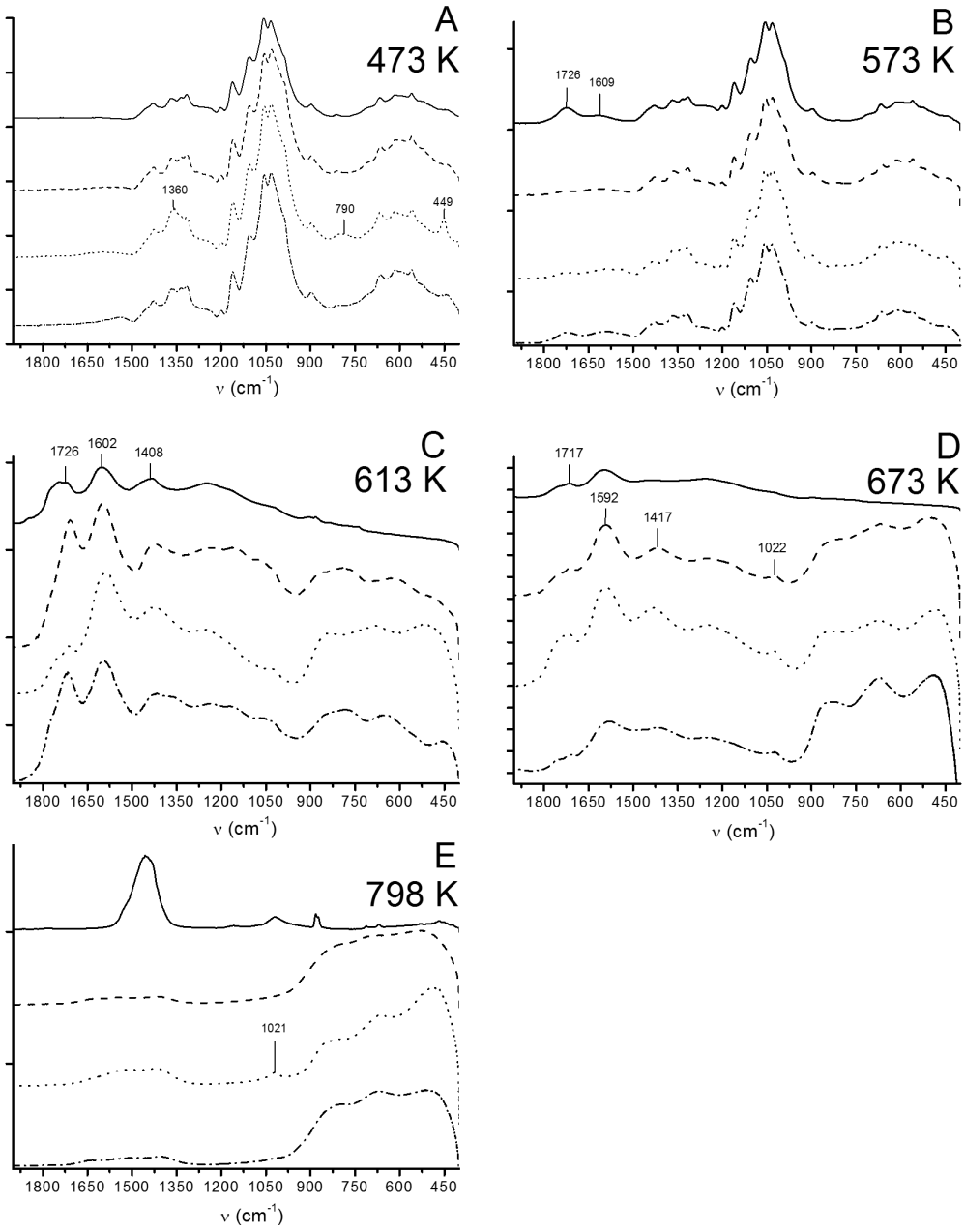

Figure 8. ATR-FTIR spectra for thermal decomposition of fully bleached Kraft pulp reference (–), and, pulps with LDH (*lss* (- - -), *hss* (· · ·) and *Uhyd* (– · –)).

A broad signal from charred products, mainly inorganic carbonates from Na, K, Ca and Mg, after oxidation of cellulose at 798 K (525 °C), appears to centre around 1450 cm^{-1} (Figure 8E). The weak and broad signal at 1021–1022 cm^{-1} (Figure 8D,E) is assigned for metal oxides while the sharp and weak dublet in reference sample close to 900 cm^{-1} in figure 8E belongs, most likely, to metal carbonates as well. Stretch vibrations from M^{II}-O-M^{III} were present only in LDH containing samples.

Combustion kinetics was evalueted by treating the samples at 613 K (340 °C) for preset time intervals. The results are presented in Figure 9. Signal evolution proceeded gradually in all LDH containing samples (Figure 9A2–C2). Reference pulp fibers charred relatively slowly (Figure 9D2). However, after

240 s the combustion kinetics increased markedly. All LDH modified samples contained organic material even after 420 s of combustion while reference pulp was practically incinerated.

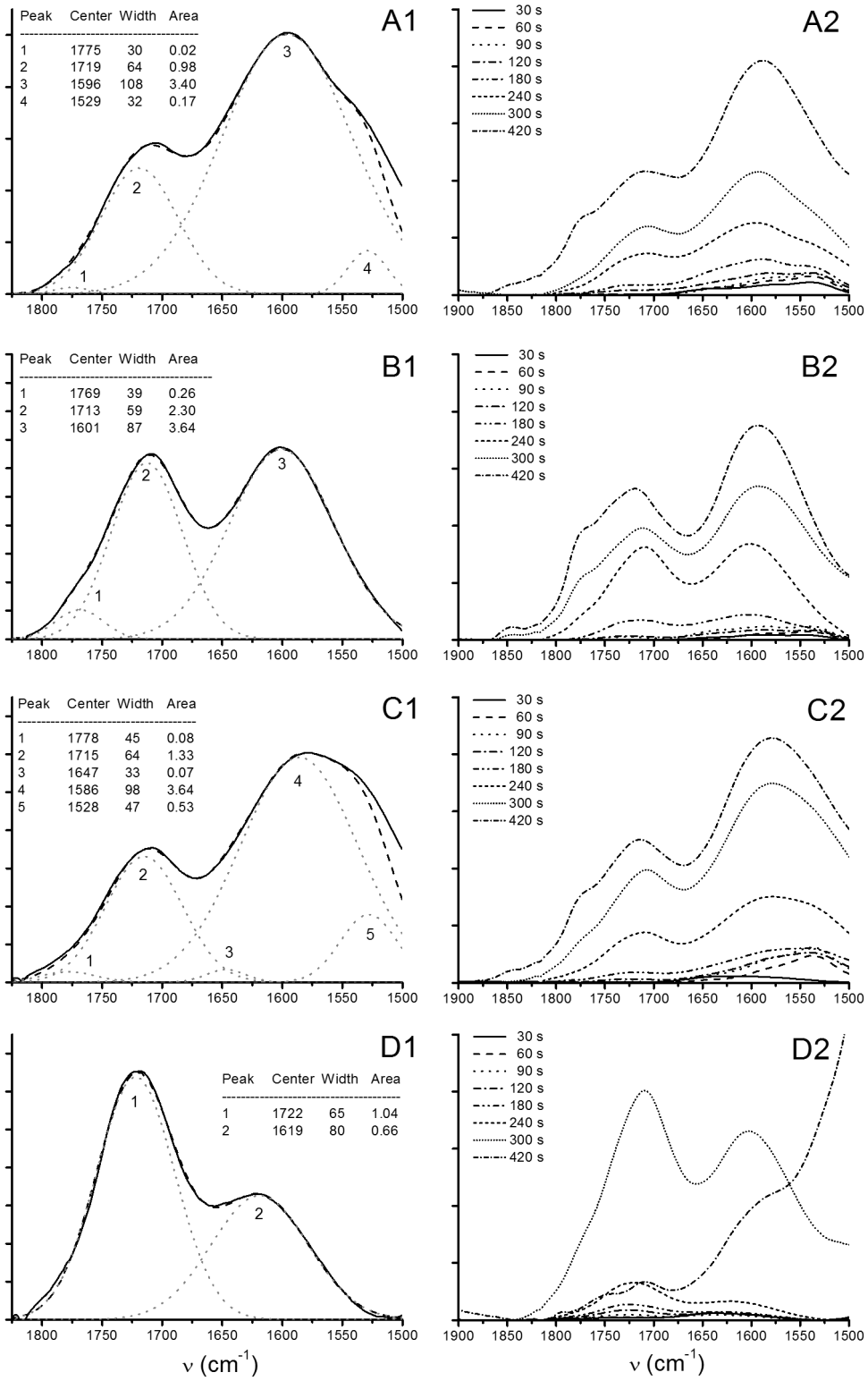

Figure 9. ATR-FTIR spectra from thermal decomposition kinetics of LDH containing pulps at 613 K (340 °C) ((**A**) *lss*; (**B**) *hss*; (**C**) *Uhyd*) and (**D**) fully bleached Kraft pulp reference. Deconvoluted FTIR spectra after 240 s in range of 1500–1850 cm^{-1} are presented in figures (**A**1–**D**1), and signal evolution within 420 s in figures (**A**2–**D**2).

Deconvoluted spectra revealed the differences in combustion kinetics in each LDH containing samples (Figure 9A1–D1). The signal at around 1585–1620 cm^{-1} arises from diones, presumambly mainly from 1,3-diketones, while the absorption at around 1775–1720 cm^{-1} is assigned as carboxylic acids, aldehydes, and 1,2-diketones [37,67]. In all LDH containing samples but specifically in those that contained fiber wall penetrated particles (*lss* and *Uhyd*) combustion produced partially oxidised cellulose in relatively high amounts. Pulp fibers without LDH were readily oxidised to carboxylic acids. We assume that the lower energy needed for aldehyde and dione formation drives the combustion in LDH containing samples due to loss of water and hydroxyls from LDH crystals. The carbonate in LDH particles contributed to the deconvoluted spectra of *lss* and *Uhyh* samples (peak numbered as 4 and 5 respectively). Similar effect with *hss* sample was observed after 300 s (Figure 9B2). Small contribution from water was also needed for the fitted curve in *Uhyd* to match the recorded absorption signals (peak number 3). The interference curve in *lss* and *Uhyd* deviates from the original below 1525 cm^{-1} due to additional signals originating from complex absorption of cellulose, and, carbonate in LDH gallery. Again we must make a note that in *lss* the contribution from nitrates should be bared in mind. We can not distinguish the fractional basis of CO_3^{2-} and NO_3^- in peak number 4 (Figure 9A1).

3.2.4. Capillary Viscometry

To address the possible depolymerisation of cellulose, the intrinsic viscosity of fibers dissolved in cupriethylene diammine (CED) was measured with the capillary viscometer. Experimental values are listed Table 4. The weight corrected limiting viscosity numbers decreased in order of Reference $>$ *hss* $>$ *lss* $>$ *Uhyd*. Slow urea hydrolysis reduced the intrinsic viscosity approximately 20%. It can be argued that neither the alkaline medium nor the existence or the amount of LDH was responsible for lowered viscosity number. The former argument is supported by the fact that the end pH was about 0.5–1.0 units higher in *hss* system than in the other two. The possibility for LDH influence was removed by measuring the viscosity of 0.5 M CED solution that contained 20 mg of HT. Viscosity in that case was unaffected. The larger LDH-U particles may have a small effect on flow properties; but, further experiments need to be performed to determine the extent of this influence. One possibility for the polymer length reduction is that the LDH is acting as a catalyst during the alkaline hydrothermal treatment. Chemisorbed particles can catalyse reactions only at the imminent fiber surface. However, the *Uhyd* and *lss* processes may catalyse hydrolysis reactions within the fiber wall as well.

3.2.5. Microrobotic Instrumentation

Experimental values from the microrobotic platform are tabulated in Tables 4 and 5. Since the LDH-C and LDH-OH nucleated mainly on the fiber surface in *hss* and *lss* synthesis, respectively, the compliances should not change significantly. The degree of polymerisation of cellulose is inversly related to fiber stiffness. Reduction in cellulose polymer length should therefore increase fiber compliance. Albeit the standard deviations in the experimented values are large, one can, nevertheless, fathom the tendency that follows. Experimental results show that *Uhyd* synthesis route reduced the fibers flexibility about 50% while *lss* and *hss* synthesis routes leave fibers unchanged. The reduction in compliance was significant according to the *T*-test as well (Table 5). Therefore the LDH particles that adsorb onto the fibers external

surface alone do not contribute to compliance in the given system. Particles that reside inside the fiber wall reduce compliance markedly.

Table 4. The experimental average compliances (k^{-1}) for untreated Kraft pulp fibers (Reference) according to Saketi *et al.* [30], and, for pulp samples from this work are presented with cellulose fraction corrected limiting viscosity numbers (η). Standard deviation for the compliances are indicated in the parentheses.

Sample	k^{-1}	η
	10^9 N^{-1} · m^{-2}	mL · g^{-1}
Reference	7.63 (6.93)	923
lss	7.93 (4.04)	813
hss	8.70 (4.21)	868
Uhyd	4.30 (1.71)	754

Table 5. The calculated *T*-test results (t) for compliance measurements and the determined probability for rejection of null hypothesis (Null). High percentile value indicates greater statistical significance between the tested specimen pairs.

Pair	t	Null (%)
Uhyd to *lss*	2.6182	98.2
Uhyd to *hss*	3.0581	99.3
lss to *hss*	0.4163	31.8

3.2.6. Adsorption Experiments

Most of the ionic groups in bleached Kraft pulp fibers originates from hexenuronic and 4-*O*-methylglucuronic acids in xylan side chains ([41,68], p. 734). Some carbonyl functionalities may reside in residual lignin as muconic acids but the number is low and their contribution to total charge may be small [69]. Fibers charge and their acid/base properties in general has been recognized to influence over many important parameters in pulp and paper manufacturing such as metal ion binding, fiber swelling and water uptake, sheet formation, tensile strength, refining response, and, floc formation together with retention aids [32,51,70,71].

The results for adsorption isotherms with MB and MY are presented in Figure 10. The ionic strength in each experiment was set with KCl and kept at 1 mM. The solution pH (8.2) was controlled with barbital buffer. At this pH the fibres are partially swollen. Determined charge in reference pulp according to MB adsorption was approximately 50 μmol·g^{-1} (Figure 10A). The LDH-C and LDH-OH particles reduced the adsorption of MB approximately 15% while LDH-U provided 35% reduction. Langmuir fitted data indicates true monolayer formation and equal site preference for both probe molecules (Figure 10B,D). For MB adsorption the fitted parameters over estimates adsorption capacity (n). The binding affinity term (K) is similar to all modified pulp fibers while for the reference it is clearly higher (Figure 10A,B). In case

of MY, the fitted parameters for equilibrium concentration followed the observed monolayer adsorption and K decreased in the order $hss > Uhyd > lss$ (Figure 10C,D). The change in solvent ionic strength above approximately 5 mM reduced adsorption significantly (Figure 10E). The adsorption phenomenon must, therefore, be controlled mainly by electrokinetic interactions. Also, the reference pulp fibers did not adsorb any MY. It seems that the more there is LDH on external fiber surface and the better the crystallinity is in LDH, the higher is the affinity towards anionic species. Induced crystalline defects, however, provide higher number of exchangeable anionic sites. These results suggest that major part of the carboxylic acids in pulp fibers are still free and that fibers have become ampholytic to a degree. The contributions from surface bound and fiber wall embedded LDH cannot be addressed at this point.

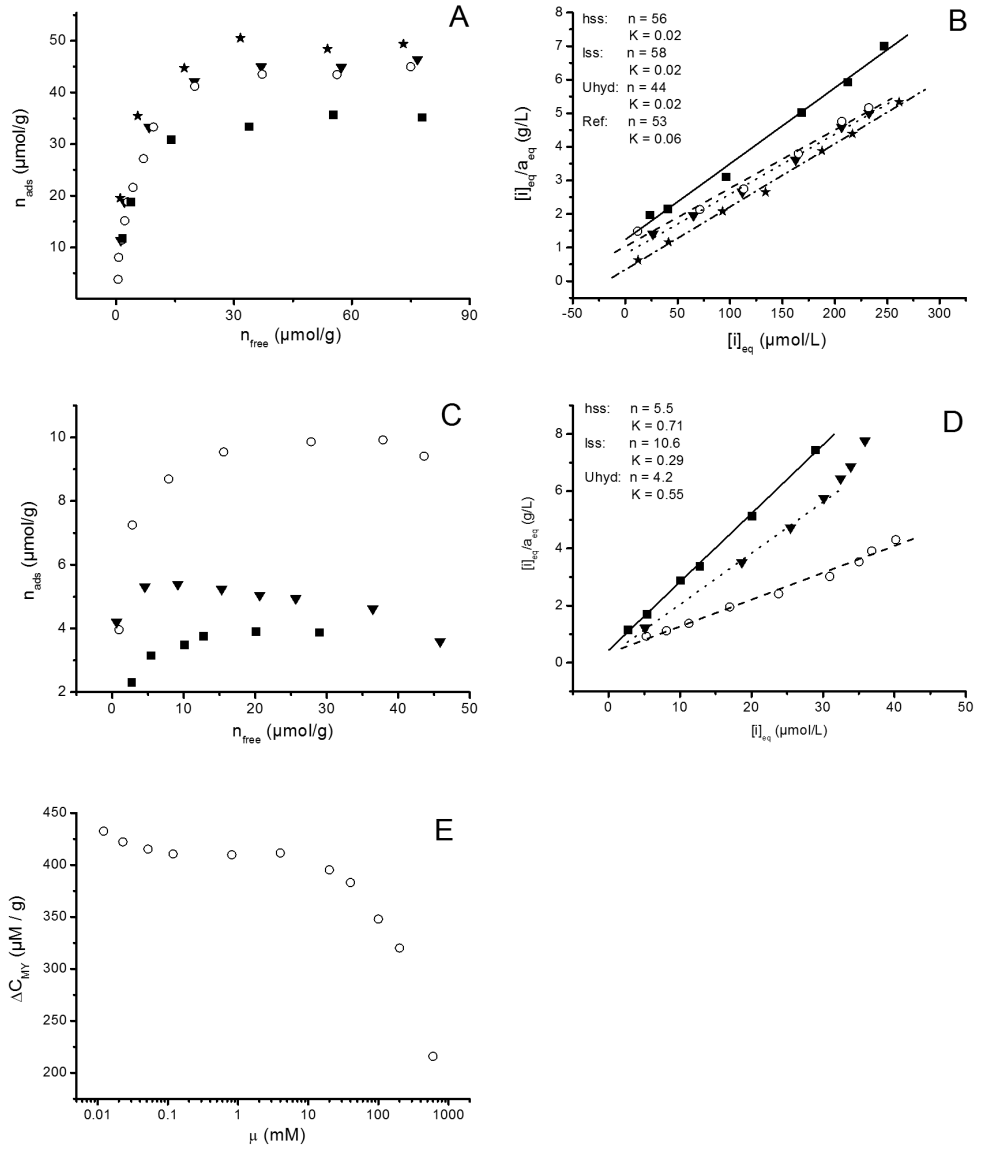

Figure 10. (**A**) Methylene Blue and (**C**) Metanil Yellow adsorption isotherms for fully bleached Kraft pulp reference (★), and LDH containing pulp samples (*hss* (▼), *lss* (◯), *Uhyd* (■)); (**B** The langmuir fit for methylene blue adsorption) and (**D**) for metanil yellow adsorption are also presented; (**E**) The effect of ionic strength on MY adsorption is shown with *lss* sample as an example.

4. Conclusions

Effective LDH particle nucleation on fiber surface was succesfully conducted in aqueous medium of low super saturated (*lss*), high super saturated (*hss*) and slow urea hydrolysis (*Uhyd*) synthesis methods. In these synthesis procedures the applied pulp fibers were acting as templates for nano- (70 nm), sub-micron (200 nm) and micron (2 μm) size LDH particles, respectively. The double layer structure of LDH was the outcome in all synthesis pathways.

Nucleation of LDH *in situ* from *hss* solvent with fully bleached Kraft pulp fibers in an autoclave does not induce particle synthesis or migration into the fiber wall, even if the fibers are fully saturated and swollen in alkaline medium (pH = 10) and elevated temperature (T = 120 °C). According to microrobotic experimentation the LDH that were bound to fibres external surface had a marginal effect on fiber flexibility. The synthesis via *lss* route resulted some particle migration into the fiber wall owing most likely to the stirring during the synthesis. However, majority of the nanoparticles remained on fiber surface. Considerable particle nucleation inside the fiber wall was discovered with TEM after hydrothermally induced urea hydrolysis (*Uhyd*) that resulted 50% reduction in bending compliance. The nucleation within the cell wall was attributed to local pH change in S2 layer.

Significant reduction in specific exothermic heat was observed after each syntesis route. Reduction cellulose polymer length influenced to the heat of combustion during the first exotherm at around 593 K (320 °C). Influence of LDH in enthalpy reduction was weight related.

Carboxylic acids are created in higher relative amounts during the slow combustion in comparison to rapid temperature increase that produces diones due, most likely, to simultaneous removal of water and hydroxyls from the LDH. The effect is amplified by the particles in fiber wall.

During the *in situ* synthesis the LDH were found to act as a catalyst in the depolymerisation reactions of cellulose in the alkaline aqueous solution. The cellulose polymerisation degree followed each synthesis in the order: *hss* > *lss* > *Uhyd*. The *Uhyd* had the greatest effect.

The LDH particles that were synthesised via *lss* method had the highest capacity for sulphate containing probe molecules while the better crystallised particles from *hss* and *Uhyd* had the highest affinity. Most of the acidic groups in cellulolse pulp fibers were free after LDH synthesis. Fibers had, therefore, become ampholytic after the modification.

Considering the results, we propose that these mineralised and surface modified fibers can be used in flame retardant, adsorbent applications and in systems where pulp fibers are modified in alkaline environment. If the catalytic activity of LDH is retained after nucleation inside the fibers cell wall there is also a possibility to modify fibers from within.

Acknowledgments

We would like to thank TEKES (Finnish Funding Agency for Technology and Innovation) for their financial support. We would also like to thank UPM-Kymmene, Stora Enso and Metsä Fiber for their financial support and Metsä Fiber Rauma mill for providing the pulp for the experiments. The research leading to these results has received funding from the WoodWisdom-Net 2 Research Programme in the project PowerBonds (Grant No.: 256527). Finally we acknowledge all the laboratory personnel at Åbo

Akademi University who assisted in laboratory experimentation, especially Jessi Mäkinen and Xiaoman Yang for their help.

Author Contributions

TEM images were provided by Mehedi Reza (Aalto University, Finland) and the microrobotic experimentation was performed by Seyed Kourosh Latifi (Tampere University of Technology, Finland) under supervision of Pasi Kallio. Mika Lastusaari (University of Turku, Finland) helped with thermogravimetric analysis. Carl Lange carried out the study, as part of his Ph.D. thesis, and was responsible for all parts of the research project including writing the manuscript. Pedro Fardim was responsible for overall supervision.

Supplementary Information

Supplementary materials can be accessed at: http://www.mdpi.com/2079-6439/3/2/0103/s1.

Conflicts of Interest

The authors declare no conflict of interest.

References

1. Leroux, F.; Besse, J.P. Polymer Interleaved Layered Double Hydroxide: A New Emerging Class of Nanocomposites. *Chem. Mater.* **2001**, *13*, 3507–3515.
2. Basu, D.; Das, A.; Stoeckelhuber, K.W.; Wagenknecht, U.; Heinrich, G. Advances in layered double hydroxide (LDH)-based elastomer composites. *Progress Polym. Sci.* **2014**, *39*, 594–626.
3. Yu, X.Y.; Luo, T.; Jia, Y.; Xu, R.X.; Gao, C.; Zhang, Y.X.; Liu, J.H.; Huang, X.J. Three-dimensional hierarchical flower-like Mg-Al-layered double hydroxides: Highly efficient adsorbents for As(v) and Cr(vi) removal. *Nanoscale* **2012**, *4*, 3466–3474.
4. Zhou, J.Z.; Wu, Y.Y.; Liu, C.; Orpe, A.; Liu, Q.; Xu, Z.P.; Qian, G.R.; Qiao, S.Z. Effective Self-Purification of Polynary Metal Electroplating Wastewaters through Formation of Layered Double Hydroxides. *Environ. Sci. Technol.* **2010**, *44*, 8884–8890.
5. Mousty, C.; Walcarius, A. Electrochemically assisted deposition by local pH tuning: A versatile tool to generate ordered mesoporous silica thin films and layered double hydroxide materials. *J. Solid State Electrochem.* **2014**, 1–27.
6. Ishizaki, T.; Chiba, S.; Watanabe, K.; Suzuki, H. Corrosion resistance of Mg-Al layered double hydroxide container-containing magnesium hydroxide films formed directly on magnesium alloy by chemical-free steam coating. *J. Mater. Chem. A* **2013**, *1*, 8968–8977.
7. Zhang, F.; Zhao, L.; Chen, H.; Xu, S.; Evans, D.; Duan, X. Corrosion Resistance of Superhydrophobic Layered Double Hydroxide Films on Aluminum. *Angew. Chem. Int. Ed.* **2008**, *47*, 2466–2469.
8. He, S.; An, Z.; Wei, M.; Evans, D.G.; Duan, X. Layered double hydroxide-based catalysts: Nanostructure design and catalytic performance. *Chem. Commun.* **2013**, *49*, 5912–5920.

9. Parida, K.; Mohapatra, L. Recent progress in the development of carbonate-intercalated Zn/Cr LDH as a novel photocatalyst for hydrogen evolution aimed at the utilization of solar light. *Dalton Trans.* **2012**, *41*, 1173–1178.
10. Liu, J.; Li, Y.; Huang, X.; Li, G.; Li, Z. Layered Double Hydroxide Nano- and Microstructures Grown Directly on Metal Substrates and Their Calcined Products for Application as Li-Ion Battery Electrodes. *Adv. Funct. Mater.* **2008**, *18*, 1448–1458.
11. Faraji, S.; Ani, F.N. Microwave-assisted synthesis of metal oxide/hydroxide composite electrodes for high power supercapacitors-A review. *J. Power Sour.* **2014**, *263*, 338–360.
12. Fan, X.; Yang, Z.; Xie, X.; Long, W.; Wang, R.; Hou, Z. The electrochemical behaviors of Zn-Al-La-hydrotalcite in Zn-Ni secondary cells. *J. Power Sour.* **2013**, *241*, 404–409.
13. Goncalves, N.A.; Caio, T.R.N.; Boaventura de Moraes, S.; Lona, L.M.F. Synthesis and characterization of biodegradable poly(L-lactide)/layered double hydroxide nanocomposites. *Polym. Bull.* **2014**, *71*, 2235–2245.
14. Dou, Y.; Xu, S.; Liu, X.; Han, J.; Yan, H.; Wei, M.; Evans, D.G.; Duan, X. Transparent, Flexible Films Based on Layered Double Hydroxide/Cellulose Acetate wiht Excellent Oxygen Barrier Property. *Adv. Funct. Mater.* **2014**, *24*, 514–521.
15. Schmidt, B.; Katiyar, V.; Plackett, D.; Larsen, E.H.; Gerds, N.; Koch, C. Bender; Petersen, J.H. Migration of nanosized layered double hydroxide platelets from polylactide nanocomposite films. *Food Addit. Contam. Part A Chem. Anal. Control Expo. Risk Assess.* **2011**, *28*, 956–966.
16. Von Haartman, S.; Heikkilä, E.; Lange, C.; Fardim, P. Potential Applications of Hybrid Layered Double Hydroxide (LDH) Particles in Pulp and Paper Production. *BioResources* **2014**, *9*, 2274–2288.
17. Winters, R.; Schomaker, E.; de Vos, S.C. Polymer-Containing Composition, Its Preparation and Use. Netherlands WO2009112441 A1, 17 September 2009.
18. Beckham, G.T.; Biddy, M.J.; Chmely, S.C.; Sturgeon, M. Hydroxide Catalysts for Lignin Depolymerization. USA US 20140107381 A1, 17 April 2014.
19. Swanson, C.; Stimpfling, T.; Troutier-Thulliez, A.L.; Hintze-Bruening, H.; Leroux, F. Layered double hydroxide platelets exfoliation into a water-based polyester. *J. Appl. Polym. Sci.* **2013**, *128*, 2954–2960.
20. Costantino, U.; Marmottini, F.; Nocchetti, M.; Vivani, R. New Synthetic Routes to Hydrotalcite-Like Compounds: Characterisation and Properties of the Obtained Materials. *Eur. J. Inorg. Chem.* **1998**, *1998*, 1439–1446.
21. Mostafa Moujahid, E.; Besse, J.P.; Leroux, F. Poly(styrene sulfonate) layered double hydroxide nanocomposites. Stability and subsequent structural transformation with changes in temperature. *J. Mater. Chem.* **2003**, *13*, 258–264.
22. Abello, S.; Mitchell, S.; Santiago, M.; Stoica, G.; Perez-Ramirez, J. Perturbing the properties of layered double hydroxides by continuous coprecipitation with short residence time. *J. Mater. Chem.* **2010**, *20*, 5878–5887.
23. Wang, J.; Fan, G.; Li, F. A hybrid nanocomposite precursor route to synthesize dispersion-enhanced Ni catalysts for the selective hydrogenation of o-chloronitrobenzene. *Catal. Sci. Technol.* **2013**, *3*, 982–991.

24. Abelló, S.; Bolshak, E.; Montané, D. Ni-Fe catalysts derived from hydrotalcite-like precursors for hydrogen production by ethanol steam reforming. *Appl. Catal. A Gen.* **2013**, *450*, 261–274.
25. Lin, J.K.; Uan, J.Y.; Wu, C.P.; Huang, H.H. Direct growth of oriented Mg-Fe layered double hydroxide (LDH) on pure Mg substrates and in vitro corrosion and cell adhesion testing of LDH-coated Mg samples. *J. Mater. Chem.* **2011**, *21*, 5011–5020.
26. Ma, S.; Wang, J.; Du, L.; Fan, C.; Yahong, S.; Sun, Y.; Sun, G.; Yang, X. Co-Assembly of LDH Nanosheets with Crown Ethers: Structural Transformation and Water-Adsorption Behaviour. *Eur. J. Inorg. Chem.* **2013**, *2013*, 1363–1370.
27. He, J.; Wei, M.; Li, B.; Kang, Y.; Evans, D.G.; Duan, X. Preparation of Layered Double Hydroxides. In *Layered Double Hydroxides*; Duan, X., Evans, D.G., Eds.; Springer-Verlag: Berlin, Germany, 2006; Volume 119, pp. 90–103.
28. Lange, C.; Lundin, T.; Fardim, P. Hydrophobisation of mechanical pulp fibres with sodium dodecyl sulphate functionalised layered double hydroxide particles. *Holzforschung* **2011**, *66*, 433–441.
29. Lange, C.; Touaiti, F.; Fardim, P. Hybrid clay functionalized biofibres for composite applications. *Compos. Part B Eng.* **2013**, *47*, 260–266.
30. Saketi, P.; Treimanis, A.; Fardim, P.; Ronkanen, P.; Kallio, P. Microrobotic Platform for Manipulation and Flexibility Measurement of Individual Paper Fibres. In Proceedings of the IEEE/RSJ International Conference on Intelligent Robots and Systems, Taipei, Taiwan, 18–22 October 2010; pp. 5764–5766.
31. Martin, A. Toward a referee viscosity method for cellulose. *Tappi J.* **1951**, *34*, 363–366.
32. Fardim, P.; Holmbom, B. Fast determination of anionic groups in different pulp fibres by methylene blue sorption. *TAPPI J.* **2003**, *2*, 28–31.
33. Evans, D.G.; Slade, R.C. Structure and Bonding. In *Layered Double Hydroxides*; Duan, X., Evans, D.G., Eds.; Springer-Verlag: Berlin, Germany 2006; Volume 119, pp. 1–87.
34. Miyata, S. Physico-chemical properties of synthetic hydrotalcites in relation to composition. *Clays Clay Miner.* **1980**, *28*, 50–56.
35. Theiss, F.L.; Ayoko, G.A.; Frost, R.L. Thermogravimetric analysis of selected layered double hydroxides. *J. Therm. Anal. Calorim.* **2013**, *112*, 649–657.
36. Hibino, T.; Yamashita, Y.; Kosuge, K.; Tsunashima, A. Decarbonation behavior of Ma-Al-CO_3 Hydrotalcite-like compounds during heat treatment. *Clays Clay Miner.* **1995**, *43*, 427–432.
37. Socrates, G. *Infrared and Raman Characteristic Group Frequencies*, 3rd ed.; John Wiley & Sons, LTD: Chichester, England, 2004.
38. Stanimirova, T.; Hibino, T.; Balek, V. Thermal behhavior of Mg-Al-CO_3 layered double hydroxide characterized by emanation thermal analysis. *J. Therm. Anal. Calorim.* **2006**, *84*, 473–478.
39. Adler, H.H.; Kerr, P.F. Infrared spectra, symmetry and structure rrelation of some carcarbon minerals. *Am. Mineral.* **1963**, *48*, 839–853.
40. Rey, F.; Fornés, V.; Rojo, J.M. Thermal decomposition of hydrotalcites. *J. Chem. Soc. Faraday Trans.* **1992**, *88*, 2233–2238.
41. Sixta, H. Pulp Properties and Applications. In *Handbook of Pulp*, Sixta H., Ed); WILEY-VCH Verlag GmbH&Co.: Weinheim, Germany, 2006; Volume 1, pp. 1009–1067.

42. Fan, G.; Xiang, X.; Fan, J.; Li, F. Template-assisted fabrication of macroporous $NiFe_2O_4$ films with tunable microstructural, magnetic and interfacial properties. *J. Mater. Chem.* **2010**, *20*, 7378–7385.
43. Stanimirova, T.; Balek, V. Characterization of layered double hydroxide Mg-Al-CO_3 prepared by re-hydration of Mg-Al mixed oxide. *J. Therm. Anal. Calorim.* **2008**, *94*, 477–481.
44. Stone, J.; Scallan, A. The Effect of Component Removal upon the Porous Structure of the Cell Wall of Wood. *Pulp Pap. Mag. Can.* **1968**, T288–T293.
45. Stone, J.; Scallan, A. A structural Model for the Cell Wall of Water-swollen Wood Pulp Fibres Based on Their Accessibility to Macromolecules. *Cell. Chem. Technol.* **1968**, *2*, 343–358.
46. Alince, B. Porosity of swollen pulp fibers revisited. *Nord. Pulp Pap. Res. J.* **2002**, *17*, 71–73.
47. Scallan, A. On Non-Solvent Water in Cellulosic Fibres as Determined by Salt Exclusion. *Cell. Chem. Technol.* **1987**, *21*, 215–223.
48. Yuichiro, S.; Takeshi, K. Swelling of pulp fibers in hot alkaline solution. *Sen'i Gakkaishi* **1962**, *18*, 595–599.
49. Gellerstedt, F.; Wå gberg, L.; Gatenholm, P. Swelling behaviour of succinylated fibers. *Cellulose* **2000**, *7*, 67–86.
50. Teleman, A.; Harjunpää, V.; Tenkanen, M.; Buchert, J.; Hausalo, T.; Drakenberg, T.; Vuorinen, T. Characterisation of 4-deoxy-β-L-threo-hex-4-enopyranosyluronic acid attached to xylan in pine kraft pulp and pulpulp liquor by ^{1}H and ^{13}CNMR spectroscopy. *Carbohydr. Res.* **1995**, *272*, 55–71.
51. Susilo, R.; Chandraghatgi, R.; Li, X.S.; Englezos, P. Iron, manganese and copper equiligria with wood fibres in single salt aqueous suspensions. *Can. J. Chem. Eng.* **2005**, *83*, 537–547.
52. Eriksson, G.; Grén, U. Pulp washing: Sorption equilibria of metal ions on kraft pulps. *Nord. Pulp Pap. Res. J.* **1996**, *11*, 164–170.
53. Su, P.; Granholm, K.; Harju, L.; Ivaska, A. Determination of equilibrium constants for sorption of metal ions to pulp by a batch method. *Nord. Pulp Pap. Res. J.* **2013**, *28*, 521–528.
54. Andersson, R.; Liden, J.; Öhman, L.O. The Donnan theory applied to pulp washing—Experimental studies on the removal of anionic substances from an assumed fiber lumen volume and from the fiber wall. *Nord. Pulp Pap. Res. J.* **2003**, *18*, 405–412.
55. Towers, M.; Scallan, A. Predicting the ion-exchange of kraft pulps using Donnan theory. *J. Pulp Pap. Sci.* **1996**, *22*, J332–J337.
56. Koukkari, P.; Pajarre, R.; Pakarinen, H. Modeling of the ion exchange in pulp suspensions by Gibbs energy Minimization. *J. Solut. Chem.* **2002**, *31*, 627–638.
57. Li, X.S.; Englezos, P. Application of the NICA-Donnan approach to calculate equilibrium between proton and metal ions with lignocellulosic materials. *J. Colloid Interface Sci.* **2005**, *281*, 267–274.
58. Bygrave, G.; Englezos, P. A thermodynamics-based model and data for Ca, Mg and Na ion partitioning in kraft pulp fibre suspensions. *Nord. Pulp Pap. Res. J.* **2000**, *15*, 155–159.
59. Athley, K.; Ulmgren, P. Interaction between divalent metal ions and oxygen-delignified kraft pulps. *Nord. Pulp Pap. Res. J.* **2001**, *16*, 204–214.
60. Yang, H.; Yan, R.; Chen, H.; Lee, D.H.; Zheng, C. Characteristics of hemicellulose, cellulose and lignin pyrolysis. *Fuel* **2007**, *86*, 1781–1788.

61. Benítez-Guerrero, M.; López-Beceiro, J.; Sánchez-Jiménez, P.E.; Pascual-Cosp, J. Comparison of thermal behavior of natural and hot-washed sisal fibers based on their main components: Cellulose, xylan and lignin. TG-FTIR analysis of volatile products. *Thermochim. Acta* **2014**, *581*, 70–86.
62. Stølen, S.; Grønvold, F. Critical assessment of the enthalpy of fusion of metals used as enthalpy standards at moderate to high temperatures. *Thermochim. Acta* **1999**, *327*, 1–32.
63. Amigó, J.; Chanh, N. DTA study of thermal combustion of textile fibers. *J. Therm. Anal.* **1975**, *7*, 183–185.
64. Navirin Vhathvarothai, J.N.; Yu, J. An investigation of thermal behaviour of biomass and coal during co-combustion using thermogravimetric analysis (TGA). *Int. J. Energy Res.* **2013**, *38*, 804–812.
65. Ditmars, D.A. Calibration standards for differential scanning calorimetry I. Zinc: Absolute calorimetric measurement of T_{fus} and $\Delta_{fus}H_m$. *J. Chem. Thermodyn.* **1990**, *22*, 639–651.
66. Zahra, C.; Zahra, A.M. The Perkin-Elmer 1020 series thermal analysis system. *Thermochim. Acta* **1996**, *276*, 161–174.
67. Lojewska, J.; Miśkowiec, P.; Lojewski, T.; Proniewicz, L.M. Cellulose oxidative and hydrolytic degradation: *In situ* FTIR approach. *Polym. Degrad. Stab.* **2005**, *88*, 512–520.
68. Dahlman, O.; Jacobs, A.; Liljenberg, A.; Olsson, A.I. Analysis of carbohydrates in wood and pulps employing enzymatic hydrolysis and subsequent capillary zone electrophoresis. *J. Chromatogr. A* **2000**, *891*, 157–174.
69. Chirat, C.; Hostachy, J.C.; Paloniemi, J.; Pelin, K.; Pohjanvesi, S.; Nordén, S.; Vesala, R.; Wennerström, M. Bleaching. In *Papermaking Science and Technology, Chemical Pulping Part 1: Fibre Chemistry and Technology*; Fardim P., Ed.; Paper Engineers Association/Paperi ja Puu Oy: Porvoo, Finland, 2011; Volume 6, p. 461.
70. Sundman, O.; Öhman, L.O. Acid/base and metal adsorption properties of CMC-type softwood Kraft ppulp of different charge. *Nord. Pulp Pap. Res. J.* **2006**, *21*, 372–381.
71. Barzyk, D.; Page, D.; Ragauskas, A. Acid Group Topochemistry and Fibre-to-Fibre Specific Bond Strength. *J. Pulp Pap. Sci.* **1997**, *23*, J59–J61.